Large eddy simulation of spark ignition in a turbulent methane jet

Guilhem Lacaze, Edward Richardson, Thierry Poinsot

Large Eddy Simulation of spark ignition in a turbulent methane jet

G. Lacaze [a], E. Richardson [b] and T. Poinsot [c]

[a] *CERFACS, 42 Avenue G. Coriolis, 31057 Toulouse cedex, France*

[b] *Combustion Research Facility, Sandia National Laboratories, P.O. Box 969 MS 9051, Livermore, CA 94551-0969.*

[c] *Institut de Mécanique des Fluides de Toulouse, CNRS, Avenue C. Soula, 31400 Toulouse, France*

Abstract

Large Eddy Simulation (LES) is used to compute the spark ignition in a turbulent methane jet flowing into air. Full ignition sequences are calculated for a series of ignition locations using a one-step chemical scheme for methane combustion coupled with the thickened flame model. The spark ignition is modeled in the LES as an energy deposition term added to the energy equation. Flame kernel formation, the progress and topology of the flame propagating upstream, and stabilization as a tubular edge flame are analyzed in detail and compared to experimental data for a range of ignition parameters. In addition to ignition simulations, statistical analysis of non-reacting LES solutions are carried out to discuss the ignition probability map established experimentally.

Key words: IGNITION, NUMERICAL COMBUSTION

1 Introduction

Ignition is a crucial phase in many practical applications where the transition from a non-reacting state to a stable burning regime is required to be fast and repeatable. The spark-ignition engine, the relight of an aircraft gas-turbine at high-altitude, and the ignition of a rocket engine are examples where ignition is critical and depends significantly on turbulence and mixture inhomogeneity effects [1].

Successful ignition may be divided into four steps: (1) efficient energy transfer from the ignition device to the gas, (2) formation of a flame kernel, (3) flame

growth and propagation and (4) stabilization.
In the context of laser and electrical spark ignition (which is the scope of the present study), many experimental and numerical investigations have been carried out to understand processes involved in spark generation following a local energy deposition. Maly and Vogel [2] and Teets et al. [3] proposed a description of the formation of the hot plasma by an electrical spark and quantified the amount of energy transmitted to the gas: 70 to 90% of the initial energy is lost by thermal conduction to the electrodes, shock wave and radiative effects. Ronney [4] made a review of the potential applications of laser ignition and comparison with standard spark plug devices. Phuoc et al. [5] present the main mechanisms leading to a flame kernel following the energy deposition by a laser (complementary studies are available in Ref. [6–8]). A more recent study of Phuoc et al. [9] shows that around 10% of the laser energy is actually transferred to the gas, energy loss is caused by shock wave expansion and radiative emission.

The generation of a viable flame kernel has been extensively studied numerically and experimentally in premixed mixtures at rest or in laminar flows [10–16]. In turbulent premixed flows, kernel initiation may fail due to excessive strain rate [17–19] and in laminar non-premixed flow, the kernel formation depends significantly on spark location [20,21]. In a turbulent non-premixed flow, the kernel initiation depends on turbulent strain rate and transport as well as on spark location [1]. Birch et al. [22] and Smith at al. [23] analyzed experimentally the probability P_{ker} of obtaining a flame kernel after a spark in a town gas jet flowing into air. They also measured the probability of having a flammable mixture at a given location: P_f. They first observed that $P_{ker} \approx P_f$ on the axis of the jet and that the zone where $P_f > 0$ extended further than the statistical region where the mixture is flammable due to mixing fluctuations. Another experimental study of Ahmed et al. [24] show that in a bluff-body configuration, $P_{ker} < P_f$ in the recirculation zones which are well-mixed. Velocity measurements suggest that in these regions, flame kernels quench due to excessive strain rate.

A successful flame kernel initiation does not lead to a successful ignition necessarily. This information is of prime importance for industrial applications. Ahmed and Mastorakos [25] and Ahmed et al. [24] have established ignition statistics in a jet and a bluff-body configurations and measured the probability of having a successful ignition following a spark: P_{ig}. These studies show that at many locations, a flame kernel is formed but is then blown-off because it fails to propagate into a region where the flame can be stabilized. The flame propagation and stabilization phases are then key processes of a successful ignition. In combustion systems where the fuel is injected as a fuel-rich mixture, the flame propagates by partially premixed and turbulent triple flame

processes [1]. Various studies of triple flames are reviewed by Lyons [26]. Triple flame stabilization is still not well understood but numerical and experimental studies suggest that a triple flame is less sensitive to strain than a pure diffusion flame and that triple flame displacement speeds can be several times greater than the laminar flame speed at stoichiometry [26].

The establishment of an ignition probability map for a real industrial burner by experimental means is both practically challenging and expensive. Few numerical studies address the problem of ignition of turbulent diffusion flames in complex configurations. Such simulations require treatment of both premixed and non-premixed combustion modes [27–30]. Richardson [31] and Richardson and Mastorakos [32] have discussed ignition of turbulent diffusion flames using a Reynolds Averaged Navier-Stokes (RANS) - Conditional Moment Closure (CMC) modeling: results suggest that the first order CMC reaction rate closure seems inadequate for such configurations. Additionally the probabilistic nature of the ignition process is not accessible through RANS analysis. Large Eddy Simulation (LES) computations of non-premixed turbulent flames are numerous [33–37] but only a few studies concern forced ignition of such flames [38,39] and further validation is required in this field.

The objective of this study is to present the LES of a spark ignition in a turbulent non-premixed jet studied experimentally by Ahmed and Mastorakos [25]. Several aspects of the flame position, flame topology and behavior obtained in the LES are compared to experimental data and discussed.

This paper proceeds with a presentation of the numerical approach used in the study (section 2). The ignition model and its coupling with the combustion model are described in section 3. Section 4 presents the computed configuration based on the experimental setup operated by Ahmed and Mastorakos [25]. The LES is validated for cold flow conditions in section 5 and finally, the ignition sequences obtained with LES are compared to experimental data and analyzed in section 6.

2 Numerical approach

The LES solver computes the compressible Navier-Stokes equations in a multi-species formulation [40–42]. For the present study, a two-step Taylor Galerkin numerical scheme [43] is used, which provides a third order accuracy in space and time. Explicit time-advancement is employed to minimize numerical dissipation.

LES for reacting flows involves the spatial Favre filtering operation that reduces for spatially, temporally invariant and localised filter functions [44], to:

$$\widetilde{f}\left(x\right) = \frac{1}{\overline{\rho}(x,t)} \int \rho(x',t) f\left(x\right) G_{\triangle}\left(x'-x\right) dx' \tag{1}$$

where $G_{\triangle}$ denotes the filter function and ρ the density.

The compressible LES equations solved by the code can be written [45]:

$$\frac{\partial \overline{\mathbf{w}}}{\partial t} + \nabla \cdot \overline{\mathbf{F}} \; = \; \overline{\mathbf{S}}_{\mathbf{c}} \tag{2}$$

where $\overline{\mathbf{w}}$ is the vector of transported variables, $\overline{\mathbf{F}}$ is the flux tensor composed of viscous, inviscid and Sub-Grid Scale (SGS) components and $\overline{\mathbf{S}}_{\mathbf{c}}$ is the chemical source term. $\overline{\mathbf{w}}$ and $\overline{\mathbf{S}}_{\mathbf{c}}$ are given respectively by:

$$\mathbf{w} = (\overline{\rho}\widetilde{u}, \overline{\rho}\widetilde{v}, \overline{\rho}\widetilde{w}, \overline{\rho}\widetilde{E}, \overline{\rho}\widetilde{Y_k})^T \;\text{ and }\; \overline{\mathbf{S}}_{\mathbf{c}} = (0,0,0,\overline{\dot{\omega}_T} + \dot{Q}, \overline{\dot{\omega}_k})^T \tag{3}$$

where $\mathbf{u} = (u,v,w)^T$ the velocity vector, the total energy per unit mass is defined by $E = 1/2\mathbf{u}\cdot\mathbf{u} + E_i$ where E_i is the internal energy and Y_k is the mass fraction of species k.

The models for the chemical production rates $\dot{\omega}_k$ and the heat release $\dot{\omega}_T$ (Eq. 3) are described later and the $\dot{Q}$ term is the ignition source term (section 3).

The LES solver takes into account changes of heat capacity with temperature and composition through tabulated thermodynamics. The multispecies fluid follows the ideal gas law: $P = \rho r T$ where P is the pressure, r the mixture gas constant and T the temperature. Viscous transport uses the classical gradient approach: the fluid viscosity follows Sutherland's law, the heat diffusion coefficient is derived from Fourier's law and the species molecular transport coefficients are obtained using a species Schmidt number along with the Hirschfelder and Curtiss approximation [45].

Application of the filtering operation to the instantaneous set of compressible Navier-Stokes transport equations with chemical reactions yields the LES transport equations [45]. The LES equations contain SGS quantities that are closed using the WALE model [46] by introducing a local turbulent viscosity ν_t. The unresolved SGS stress tensor $\overline{\tau_{ij}}^t$ is modeled using the Boussinesq approximation [47–49]:

$$\overline{\tau_{ij}}^t - \frac{1}{3}\overline{\tau_{kk}}^t \delta_{ij} = -2\overline{\rho}\,\nu_t\,\widetilde{S}_{ij} \tag{4}$$

where $\widetilde{S}_{ij}$ is the resolved strain rate tensor.

The SGS species fluxes $\overline{J_i^k}^t$ are modeled using a species SGS turbulent diffusivity $D_k^t = \nu^t / Sc_k^t$, where Sc_k^t is the turbulent Schmidt number ($Sc_k^t = 0.7$ for all species):

$$\overline{J_i^k}^t = -\overline{\rho} \left(D_k^t \frac{W_k}{W} \frac{\partial \widetilde{X_k}}{\partial x_i} - \widetilde{Y}_k V_i^c \right) \tag{5}$$

where W and W_k are the molecular weights of the mixture and of the species k respectively. X_k is the molar fraction of species k and V_i^c is the diffusion correction velocity (to ensure global mass conservation) resulting from the Hirschfelder and Curtiss approximation [45].

The SGS energy flux $\overline{q_i}^t$ is modeled:

$$\overline{q_i}^t = -\lambda_t \frac{\partial \widetilde{T}}{\partial x_i} + \sum_{k=1}^{N} \overline{J_i^k}^t \, \widetilde{h}_s^k \tag{6}$$

where the SGS turbulent thermal conductivity $\lambda_{th}^t = \overline{\rho}\, \nu^t\, C_p / Pr^t$ with Pr^t a turbulent Prandtl number ($Pr^t = 0.7$) and C_p the heat capacity at constant pressure of the mixture. $\widetilde{h}_s^k$ stands for the sensible enthalpy of species k.

The chemical source terms are modeled using the Arrhenius law via a global one-step chemical scheme (Table 1) (called MP1 in the rest of the text):

$$\dot{\omega}_{CH_4} = A\, T^{\beta}\, Y_{CH_4}^{\gamma_{CH_4}}\, Y_{O_2}^{\gamma_{O_2}} \exp\left(-\frac{Ea}{RT}\right) \tag{7}$$

Reaction	**A [cm^3/mole.sec]**	β	**Ea [cal/mole]**
$CH_4 + 2O_2 \Rightarrow CO_2 + 2H_2O$	6.9E+14	0.0	31.588E+3
forward reaction orders: γ_{CH_4}= 1.0 and γ_{O_2}= 1.0			

Table 1
Arrhenius parameters of the one-step chemical scheme MP1.

Premixed one-dimensional flames have been computed to compare the MP1 scheme with a complex scheme (325 reactions and 53 species) established by GRI (called GRI. 3.0) [50] and various experimental data from the literature. With such a simple chemical scheme, only the laminar flame speed in lean conditions can be correctly predicted. To recover the right flame speed in rich regimes, the pre-exponential constant (A) of the Arrhenius rate is changed into a function of the local equivalence ratio ϕ [51,52]: $A(\phi) = A \cdot$

$[1/2\,(1 + tanh\,((\phi_c - \phi)/\Delta_\phi))]^2$, with $\phi_c = 1.25$ and $\Delta_\phi = 0.2$. Adiabatic temperature and laminar flame speed are presented on Fig. 1 and compared to the detailed mechanism and experimental data. For lean conditions, the temperature of the burned gases is well predicted by MP1 (Fig. 1a) but for rich mixtures the error between MP1 and GRI 3.0 is around 10%. Laminar flame velocities are correctly predicted for all equivalence ratios (Fig. 1b).

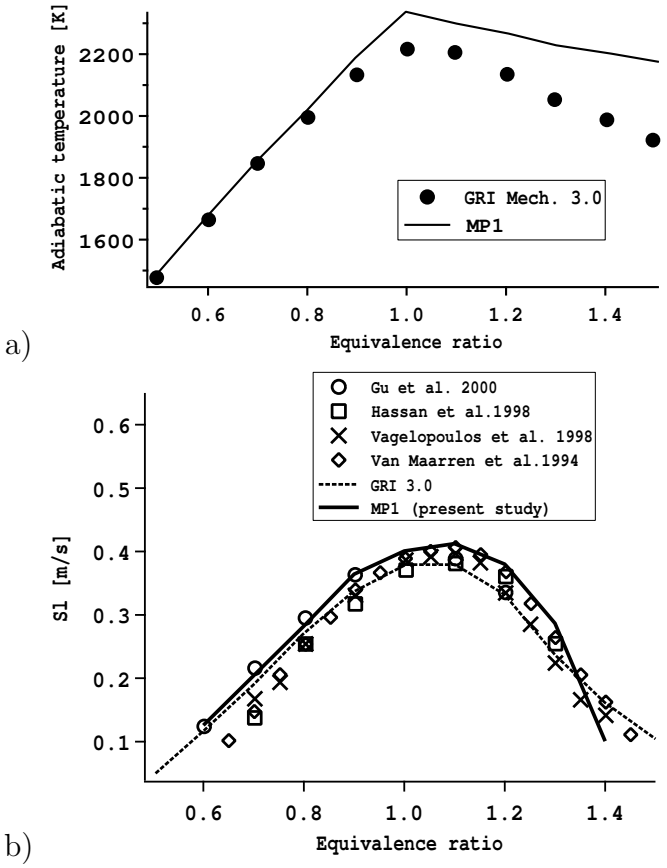

Fig. 1. Premixed laminar flame: comparison between MP1 and GRI 3.0: (a) Adiabatic temperature and (b) Laminar flame velocity (S_l), experimental measurements of Van Maaren et al. [85], Vagelopoulos et al. [86], Hassan et al. [87] and Gu et al. [88] are also given here.

The interaction between chemical kinetics and turbulence is modeled by the Dynamically Thickened Flame (TFLES) model [53]. On the basis of the theory of laminar premixed flames [54], the flame speed S_L^0 and the flame thickness δ_L^0 may be expressed as:

$$S_L^0 \propto \sqrt{D_{th}\,A} \qquad \text{and} \qquad \delta_L^0 \propto \frac{D_{th}}{S_L^0} = \sqrt{\frac{D_{th}}{A}} \tag{8}$$

where D_{th} is the thermal diffusivity and A the pre-exponential constant of the one-step chemical scheme.

Increasing the thermal diffusivity by a factor F, the flame speed is kept unchanged if the preexponential factor is decreased by the same factor [55]. This operation leads to a flame thickness which is multiplied by F and easily resolved on a LES mesh. Subgrid scale effects are introduced through an efficiency function E to reproduce the subgrid wrinkling [53,56,57]. To extend the model to partially premixed and non-premixed combustion, a sensor S (constructed as a reaction rate) is used to trigger the TFLES model only in reactive areas without affecting inert mixing away from the flame front [40,57,58]. Finally, in non-reactive regions ($S = 0,\ F = 1,\ E = 1$), standard LES equations (without chemical source terms) apply and in the flame front ($S = 1$), thickened equations apply, with: $\dot{\omega}_k^{flame} = E\,\dot{\omega}_k/F$, $D_{th}^{flame} = E\,F\,D_{th}$ and $D_k^{flame} = E\,F\,D_k$. In the flame region, the thickening factor depends on the local characteristic grid size Δ_x: $F = N_c\,\Delta_x/\delta_L^0$ where N_c is the number of points used to resolve the flame front ($N_c = 5$ to 10).

Although this approach is still being developed and requires further validations, its simplicity and its success in prior applications [40,58,59] suggest its suitability for the problem addressed in this work where the propagation and stabilization processes of the turbulent lifted flame involve premixed and diffusion combustion regimes [26].

3 A model for laser and electrical spark ignition

To capture the right flame response due to velocity and mixture fraction fluctuations at the electrode's tips, the energy deposition (ED) ignition model describes the spark as a source term added to the energy equation letting the LES solver explicitly compute the formation of the initial kernel. Even though this method requires significant simplifications of the physics taking place during the kernel formation, it is able to represent the ignition dependence on mixing, predicting for example failed ignition events if the composition at the spark location is beyond flammability limits or becomes nonflammable during the ignition event. This approach has been used in several Direct Numerical Simulations (DNS) to study the early times of flame generation [18,60,61].

The source term is described by three parameters: the energy transmitted to the gas ε_i, the duration Δ_t and the characteristic size Δ_s of the spark.

Standard CFD codes can not simulate plasma thermodynamics. Instead, the ED model seeks to deliver the energy profile that would exist following a real spark once the temperature has subsided below the ionization temperature, thus ignoring the plasma phase [2,5,7,9,62] (Fig. 2).

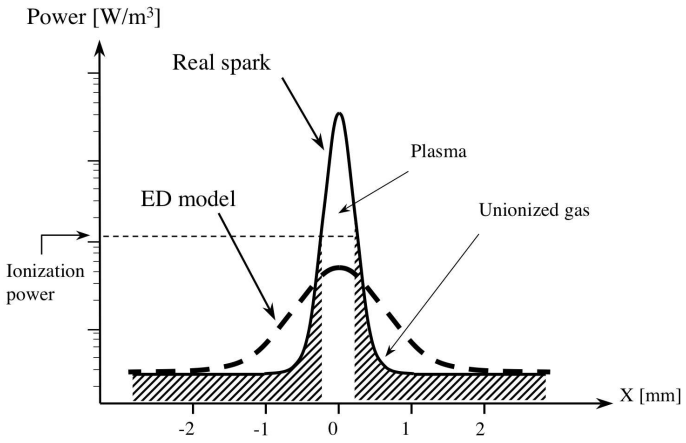

Fig. 2. Sketch of power distributions for a real spark and for the ED model.

The volumetric source term $\dot{Q}$ modeling the spark is directly added to the energy equation and is defined as a Gaussian distribution in time and space:

$$\dot{Q}(x,y,z,t) = \frac{\varepsilon_i}{4\pi^2\sigma_s^3\sigma_t} e^{-\frac{1}{2}(\frac{r}{\sigma_s})^2} e^{-\frac{1}{2}(\frac{t-t_0}{\sigma_t})^2} \tag{9}$$

where the transmitted energy ε_i corresponds to about 10% of the total energy of a laser [9] and to 10 to 30% of the overall energy of an electrical spark [2,3]. For laser-ignition, most of the initial energy ($\approx 90\%$) is lost in the generated shock wave and by radiative effects [9] whereas for an electrical spark, losses are mainly due to thermal conduction to the electrodes, radiation and shock wave expansion [2,3]. In Eq. 9, r is the distance to the center of the spark, t_0 is the moment when the power density reaches its maximum value and σ_s and σ_t are parameters that control the size and the duration of the source term defined by:

$$\sigma_s = \frac{\Delta_s}{a} \quad , \quad \sigma_t = \frac{\Delta_t}{a} \tag{10}$$

where the characteristic size Δ_s and the duration Δ_t of the deposition are divided by a factor $a = 4\sqrt{ln(10)}$ set to obtain 98% of the deposited energy in the domain $\Delta_s^3 \times \Delta_t$, or written mathematically: $\int_{\Delta_s^3}\int_{\Delta_t} \dot{Q}\ dt\ dV = 0.98 \int_{-\infty}^{+\infty}\int_{-\infty}^{+\infty} \dot{Q}\ dt\ dV$.

In the ED model, the size of the deposition Δ_s is not the distance between electrodes or the plasma volume induced by a laser. Δ_s is chosen so that the maximum temperature at the kernel centre ($r = 0$) in the absence of any heat losses does not exceed a fixed temperature T_{k_max} which is evaluated by:

$$T_{k\_max} \approx \frac{1}{\rho C_p} \int_{-\infty}^{+\infty} \dot{Q}(r=0)dt + T_0 = \frac{1}{\rho C_p} \frac{\varepsilon_i}{(2\pi)^{3/2}\sigma_s^3} + T_0 \tag{11}$$

where ρ, C_p and T_0 are respectively the density, the heat capacity at constant pressure and the temperature in the unburned gas. An estimate of Δ_s is then:

$$\Delta_s \approx \left(\frac{a}{\pi}\right)^{1/2} \left(\frac{\varepsilon_i}{\rho C_p (T_{k\_max} - T_0)}\right)^{1/3} \tag{12}$$

For $T_{k\_max} = 3000K$, Δ_s is usually of the order of two to three times the electrode distance. This procedure allows deposition of the correct total energy without reaching excessive temperatures at the spark center.

Since the ED and the TFLES models work directly on the energy equation, their coupling is straightforward: the ED model deposits energy and when the temperature is high enough (and if the mixture is flammable), the finite rate chemistry begins and a flame kernel is initiated. The only complication is the thickening which is handled as follows: thickening is not applied during the first instants of the ignition and is only triggered when a real flame starts developing. The triggering criterion is based on the mass fraction of a burnt species: thickening starts when the maximum value of the mass fraction of a product species (water in the present study) Y_{max} reaches a crossover value (Y_c) corresponding to 90% of the product mass fraction at chemical equilibrium. Figure 3 presents the temporal evolution of the maximum temperature in the domain and the value of the thickening factor in the reaction zone.

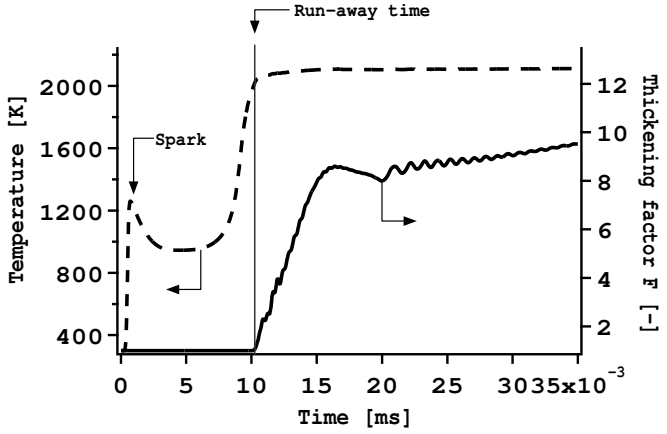

Fig. 3. Temporal evolution of the maximum temperature and maximum value of the thickening factor on a "LES" mesh with the ED-TFLES coupling. Ignition in a one-dimensional domain of a $H_2 - O_2$ mixture at an equivalence ratio of 4.

Tests on the cut-off value Y_c have shown that when Y_c changes from 70 to 95% of the equilibrium product mass fraction, the change to the ignition delay is less than 5%.

The ED-TFLES has been tested in multiple cases: ignition in 1D flows, ignition in a 3D laminar configuration (Fig.4) representing the experiment of Erard et

al. [63] (a perfectly premixed spherical flame ignited by an electrical spark) or in a rocket like experiment of DLR [39] (ignition by a laser in a non premixed H_2/O_2 flow simulating a delayed ignition in a rocket engine). It is tested here in simulation of the well controlled turbulent experiment of Ahmed and Mastorakos [25].

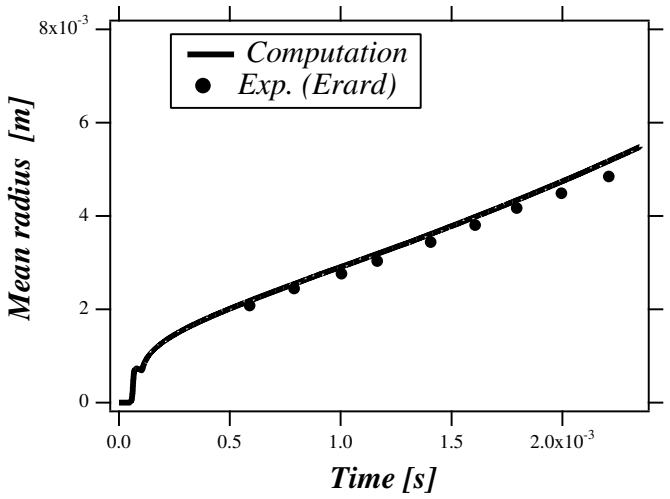

Fig. 4. Kernel radius as a function of time. Points: experimental results of Erard [63], line: calculation.

4 Configuration: a turbulent non-premixed jet

The jet configuration of Ahmed and Mastorakos [25] provides measurements in a well characterized flow: the authors report the ignition probability for a variety of spark characteristics and positions, where the ignition probability is the likelihood that a particular spark event results in the establishment of a viable flame kernel and subsequent propagation leading to a stabilized lifted flame. Fast camera and $OH\ P-LIF$ (Planar Laser-induced Fluorescence of the OH radical) records of the propagation phase are of particular interest for comparison with numerical simulation.

The jet configuration is shown in Fig. 5. A $5mm$ diameter (d_j) jet of fuel (70% of CH_4 and 30% of air in volume) with a bulk velocity of $25.5ms^{-1}$ issues into a 200 mm diameter co-flow of air moving at $0.1ms^{-1}$. The Reynolds number of the jet is $Re_j = 5800$. The jet pipe extends to $130d_j$ upstream of the nozzle so that the internal flow is expected to exhibit a fully developed turbulent velocity profile. The authors measured the mean and fluctuating velocity components for a pure air jet. Hot-wire measurements were not carried out with the methane jet because density variations and conductivity fluctuations would have induced errors. The experimental records show that the apparatus produces a jet closely matching the empirical equations describing the behavior of non-reacting jets [64].

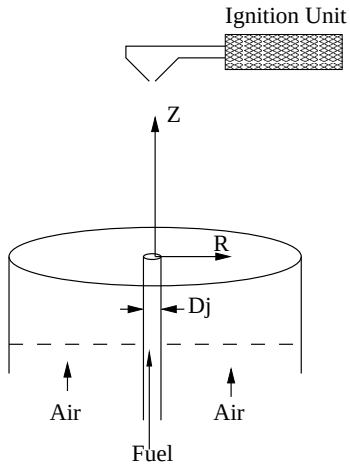

Fig. 5. Schematic diagram of the turbulent jet burner with the spark electrodes [25].

Six simulations are presented here for the Ahmed and Mastorakos experiment (Table 2). Case A: the flow dynamics are validated in an air jet configuration, numerical results are compared to hot-wire measurements carried out by Ahmed and Mastorakos. Case B: a non-reactive calculation of the methane jet has been done to validate mixing. Cases C0, C1, C2 and C3 are four ignition computations where the ED model is triggered at three different locations as in [25]. The non-reactive Cases A and B are presented in section 5 and the ignition sequence (Cases C0, C1, C2 and C3) is then studied in section 6.

Case	Validation goal	Jet injection conditions	Spark location	Experimental Data [25]
A	Flow dynamics	mixture: air $U_{mean} = 21\ m/s$ $Re = 6800$	no spark	yes
B	Mixing	mixture: $70\%\ CH_4 + 30\ \%air$ $U_{mean} = 25.5\ m/s$ $Re = 5800$	no spark	no
C0	Ignition	mixture: $70\%\ CH_4 + 30\ \%air$ $U_{mean} = 25.5\ m/s$ $Re = 5800$	$z = 50d_j\ ;\ r = 0d_j$	no
C1			$z = 40d_j;\ r = 0d_j$	yes
C2			$z = 30d_j;\ r = 0d_j$	yes
C3			$z = 4d_j;\ r = 1d_j$	yes

Table 2
Details of the jet simulations.

A pair of electrodes was positioned at various locations throughout the flow [25]. A spark with an overall duration of $400\mu s$ and a nominal electrical energy of $100mJ$ with an electrode spacing of $1mm$ and tip diameters of $0.1mm$ was used.

In the calculations, the domain is extended to a diameter of 1000 mm to avoid interaction between the jet and boundaries (Fig. 6). The injection tube is 10 mm long with a diameter of 5 mm as in the experiment. The rim of the tube is tapered at a half cone angle of 5.2 °. Figure 7 presents the tetrahedral mesh (Table 3) on a cutting plane through the domain and a close up of the jet region.

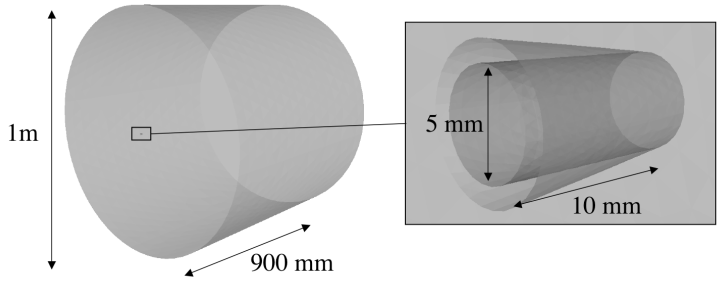

Fig. 6. Computational domain and an enlargement of the injection tube.

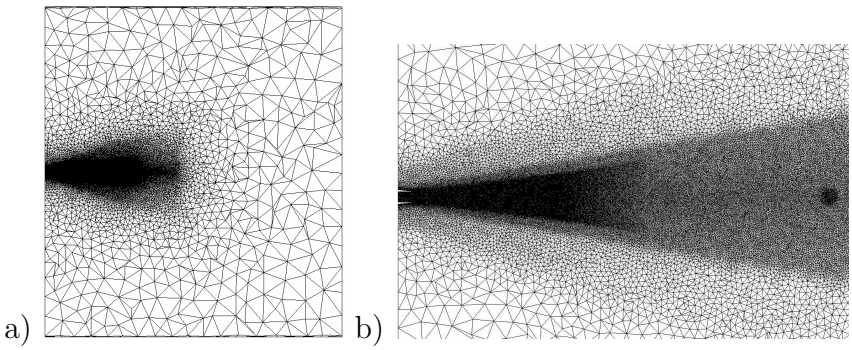

Fig. 7. a) The whole grid, b) the refined jet area.

Number of nodes	Number of cells	cell size in the tube
2,080,000	12,180,000	0.002 mm ($\approx 1/20\ d_j$)

Table 3
Characteristics of the computational mesh.

Boundary conditions are summarized in Table 4 and Fig. 8. The parameters of the boundary conditions for the three cases A, B and C are shown in Table 2.

According to section 3, the total amount of energy deposited by the ED model ($10\ mJ$) should be about 10% of the spark energy of the experiment due to large conductive and radiative losses [2,3]. The diameter of the deposition $\Delta_s \approx 3\ mm$ is estimated using Eq. 12, with a maximum temperature T_{k_max} of

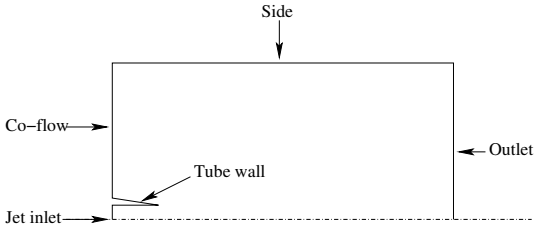

Fig. 8. Sketch of the boundary conditions of the domain.

Boundary Patch	Description
Jet Inlet	Characteristic inlet condition without turbulence injection. $1/7^{th}$ Power law mean velocity profile
Co-flow	Characteristic inlet condition
Sides	Adiabatic slip wall
Outlet	Characteristic outlet condition relaxed to the atmospheric pressure: 1.013 bar
Tube wall (inside)	Adiabatic no slip wall
Tube wall (exterior)	Law of the wall condition

Table 4
The boundary conditions of the calculation domain.

3500 K. The duration of the deposition is 400 μs as in the experiment. To have a sufficient grid resolution at the spark location (1D resolution tests showed that a minimum of five grid points in the deposition diameter is required), a mesh with a refined area ($D_x = 0.2\ mm$) at the deposition point is used to compute the ignition and early kernel propagation (Fig.7-b). A comparison between the experimental spark and the LES spark is summarized in Table 5.

	Energy amount	duration	spark width
	mJ	μs	mm
experimental spark parameters	100	400	1
simulation energy deposition parameters	10	400	3

Table 5
Parameters of the experimental and model sparks.

All computations have been performed on a *SGI ALTIX ICE 8200* cluster at the CINES computing center (France). This high-bandwidth low-latency network is equipped with 12,000 *Quad-Core E5472* processors. The LES calculations were computed over 1,000 processors on which an entire ignition sequence (900 ms of physical time) took 298,000 CPU hours.

5 Cold flow validation: Velocity and mixture fraction fields

To assess the quality of the LES, the flow field is evaluated for an air jet configuration (Case A in Table 2). Ahmed and Mastorakos [25] also carried out this first validation step. No measurement of the axial velocity on the axis of the jet is reported in Ref. [25] however, and simulation results are compared to the empirical relationship established by Tieszen et al. [64] for turbulent air jets:

$$\frac{U_m(z)}{U_j} = 11.8 \left(\frac{r_j}{z}\right) \exp\left[-93.7 \left(\frac{r}{z}\right)^2\right] \tag{13}$$

where U_m is the mean flow axial velocity on the jet axis, U_j the mean axial velocity at jet exit, r_j is the radius of the injection tube ($r_j = 2.5\ mm$) and z and r are the longitudinal and the radial coordinates ($z = 0$ at the jet exit).

Figure 9 shows that the agreement between the mean axial velocity and the correlation of Tieszen et al. is satisfactory, with shear generated turbulence penetrating to the center line at 4.5 diameters.

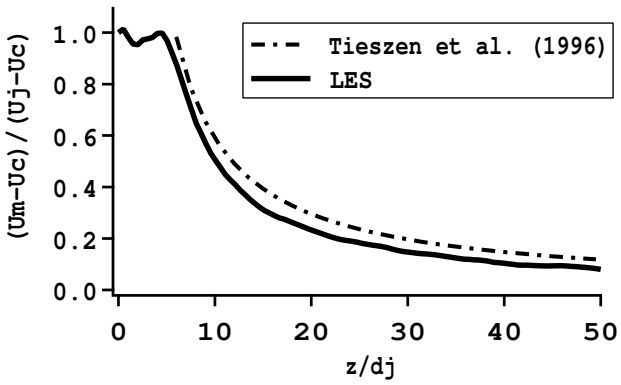

Fig. 9. Evolution along the jet axis of the mean axial velocity U_m (dashed line: Correlation of Tieszen et al. [64], solid line: LES). Air jet velocity: $U_j = 21\ m/s$ and co-flow velocity: $U_c = 0.1\ m/s$.

Figure 10 presents a comparison between different experimental hot-wire measurements and the computation of the longitudinal turbulence intensity on the axis of the jet. At the location where transition to turbulence occurs ($4.5 < z/d_j < 8$), the values of the longitudinal turbulence intensity measured in the LES are nearly two times greater than those measured in the experiments used for the comparison [65,66]. The explanation of this observation is still an open question. However, in the self-similar region ($z/d_j > 20$) where the flame develops, the results from the simulation are in the range of experimental hot-wire measurements, with an asymptotic value of the longitudinal turbulence intensity of the order of 25%.

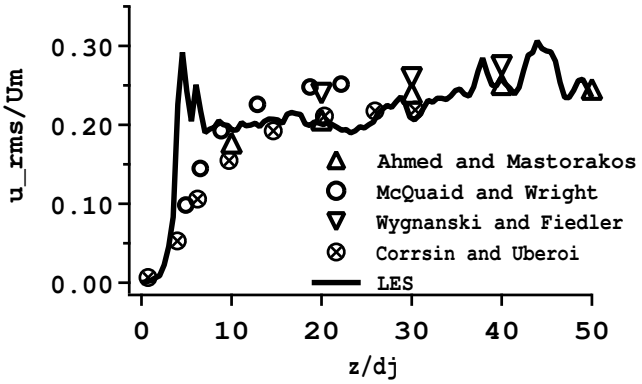

Fig. 10. Evolution along the jet axis of the axial rms-fluctuation u_rms (scaled by the mean axial velocity along the jet axis U_m), symbols: hot-wire measurements in round air jets flowing in air ($\triangle$: Ahmed and Mastorakos [25], $\circ$: McQuaid and Wright [65], $\triangledown$: Wygnansky and Fiedler [89] and $\otimes$: Corrsin and Uberoi [66]) and solid line: LES.

Figure 11 shows that the spreading angle of the jet is well captured by LES as well as the self-similar behavior of the mean axial velocity profiles in the self-preservation region ($z/d_j > 20$).

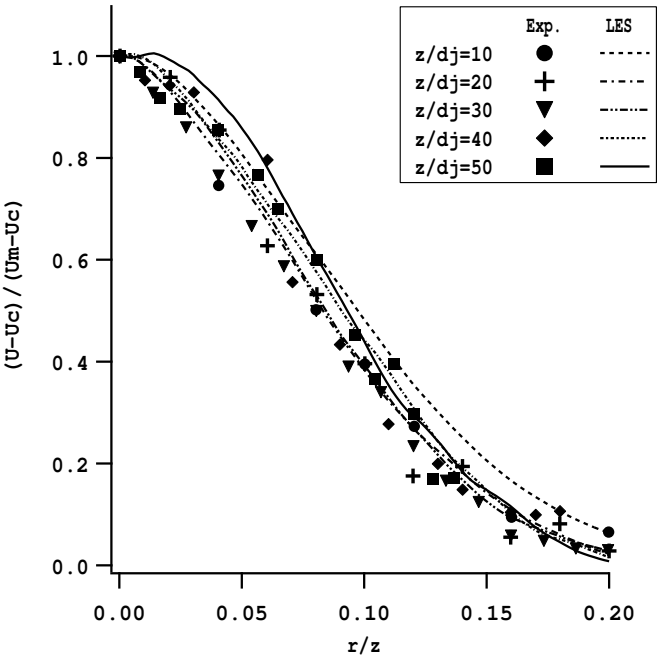

Fig. 11. Radial distribution of the mean axial velocity (U) scaled by the mean axial velocity on the axis (U_m), comparison of the experimental data of Ahmed et al. [25] (symbols) and LES results (lines). Air jet, injection velocity: $U_j = 21\ m/s$ and co-flow velocity: $U_c = 0.1\ m/s$.

Figure 12 presents the radial distribution of the streamwise fluctuations of the velocity at five downstream positions. Numerical results are in the range of

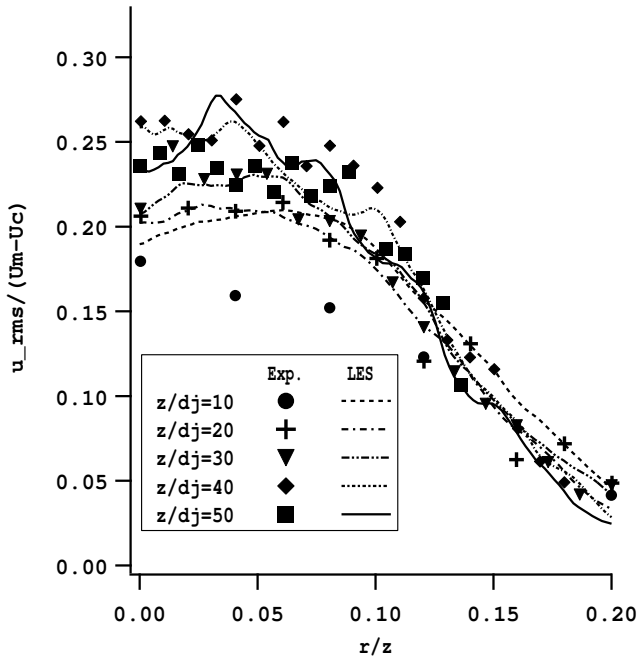

Fig. 12. Radial distribution of the axial velocity fluctuation (u_rms) scaled by the axial velocity on the axis (U_m), comparison of the experimental data of Ahmed et al. [25] (symbols) and LES results (lines). Air jet, injection velocity: $U_j = 21\ m/s$ and co-flow velocity: $U_c = 0.1\ m/s$.

experimental measurements. In the simulation, no turbulence is injected at the inlet and the velocity profile follows a $1/7^{th}$ power law. The differences observed for measurements carried out at $z/d_j = 10$ still have to be explained. Note that the direct comparison of filtered LES fields with experimental data is relevant since the subgrid scale kinetic energy k_{sgs} represents less than 7% of the total turbulent kinetic energy: $k_{tot} = k_{res} + k_{sgs}$ (where k_{res} is the resolved kinetic energy) at the five downstream positions of Fig. 12.

An additional analysis to assess the quality of the LES consists in comparing the LES grid size Dx with the different turbulent scales: the integral length scale L_t containing the maximum of the turbulent energy and the Kolmogorov length scale η_k characterizing the smallest eddies. In a round jet $L_t \approx d_j(1 + B \cdot z)$ where $B \approx 0.09$ is the expansion rate of the jet [48] and z the axial coordinate. The local Kolmogorov scale can be estimated as $\eta_k = L_t Re_t^{-3/4}$ where $Re_t = u' L_t/\nu$ is the local turbulent Reynolds number [48] obtained using the LES RMS field of velocity u' and the kinematic viscosity of the flow ν. The comparison of these characteristic sizes is shown on Fig. 13 where it is observed that in the zone of interest (i.e. for $z < 50 d_j$), the grid size represents less than 6% of the integral length scale and is only about 25 times greater

than the Kolmogorov length scale.

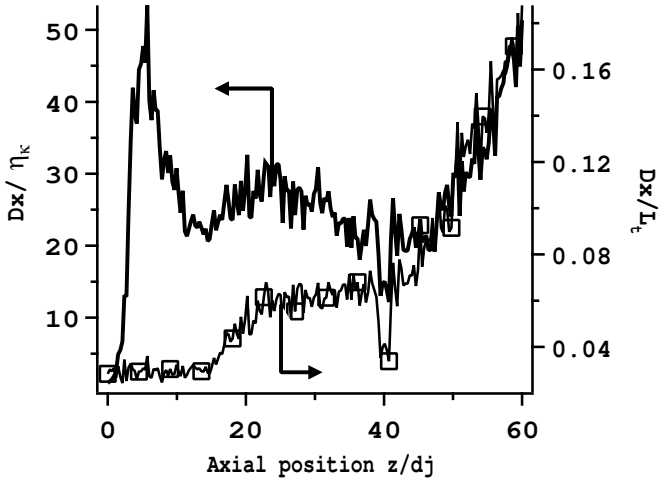

Fig. 13. Characteristic size of the LES mesh (Dx) compared to the integral scale (L_t) and the Kolmogorov scale (η_k) on the jet axis.

Case B corresponds to cold conditions before ignition (see Table 2) and is used to investigate the mixture fraction field before energy deposition. Ahmed and Mastorakos [25] did not measure the mixing of this jet and an empirical fit of Richards and Pitts, established for variable density jets [67], is again compared to LES results. Figure 14 presents the positions of three equivalence ratio iso-lines from the LES compared to the empirical law of Richards and Pitts [67]:

$$\frac{Y(r,z)}{Y_j} = 9.52 \left(\frac{\rho_j}{\rho_c}\right)^{1/2} \left(\frac{r_j}{z - 7.2 r_j}\right) \exp\left(-59 \left(\frac{r}{z - 7.2 r_j}\right)^2\right) \tag{14}$$

where $Y(r,z)$ and Y_j are respectively the mass fractions of methane in the domain and in the injection tube.

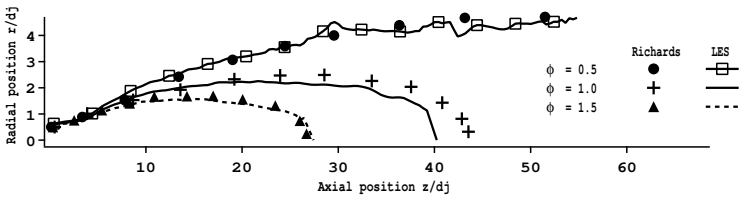

Fig. 14. Iso-lines of the equivalence ratio: comparison of LES results with the empirical law of Richards et al. [67]. Methane jet, injection velocity: $U_j = 25.5\ m/s$ and co-flow velocity: $U_c = 0.1\ m/s$

On Fig. 14, the three iso-lines are the lean and rich flammability limits of methane (respectively $\phi = 0.5$ and $\phi = 1.5$) and the stoichiometric line ($\phi = 1$). Mean LES results have been obtained from an average over 200 ms. A

satisfactory agreement is observed between numerical data and the empirical prediction.

Figure 15 plots the time evolutions of the equivalence ratio and axial velocity versus time at the spark location, here for case C1: $z = 40d_j$ and $r = 0d_j$, before ignition. The spark duration is also added to the figure as a reference. This plot shows that at the spark location both axial velocity and equivalence ratio fluctuate with time scales which are of the order of the spark duration. Hence for the present case, the use of the ED model is appropriate. Another aspect is that the value of the equivalence ratio is some times out of the flammable zone. This may lead to a reduced ignition probability. This point is discussed in the following section.

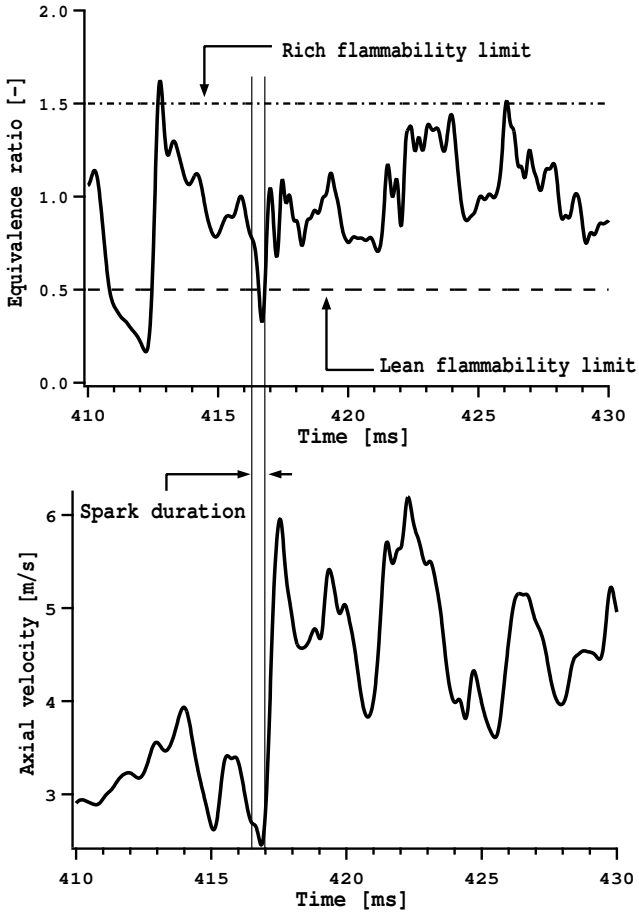

Fig. 15. Resolved equivalence ratio and axial velocity variation at the ignition location ($z = 40dj$ and $r = 0dj$) in the LES.

6 Ignition simulations: Case C

In this section the LES results of Cases C0, C1, C2 and C3 (Table 2) are first compared to experimental data of Ahmed and Mastorakos [25] and then used to analyze the progress of ignition events. The experimental ignition probabilities are discussed with reference to the velocity and mixing fields.

6.1 LES and experiment comparison

In the experiment [25] the axial position of the most upstream flame point has been determined with high speed photography and OH-PLIF images. Both diagnostics gave similar results. Ten sets of images were used to plot the average position of the upstream flame point and a maximum variation of 9% of its location at a given time was obtained. Figure 16 compares the average positions obtained experimentally with single LES realizations for cases C1, C2 and C3. In the LES, the flame location corresponds to the axial coordinate of the most upstream point of the 1500 K iso-surface. The LES flame locations agree well with those recorded in the experiment and the lift-off height is also captured. LES results fluctuate around experimental measurements, as expected, due to the fact that for each case only one LES realization is used for comparison. Note that for case C3, each upstream position of the flame in the experiment has been extracted from three pictures of Ref. [25] and is not averaged over 10 realizations. In addition, during case C0, a kernel is initiated leading to a flame that fails to propagate upstream and is then blown-off.

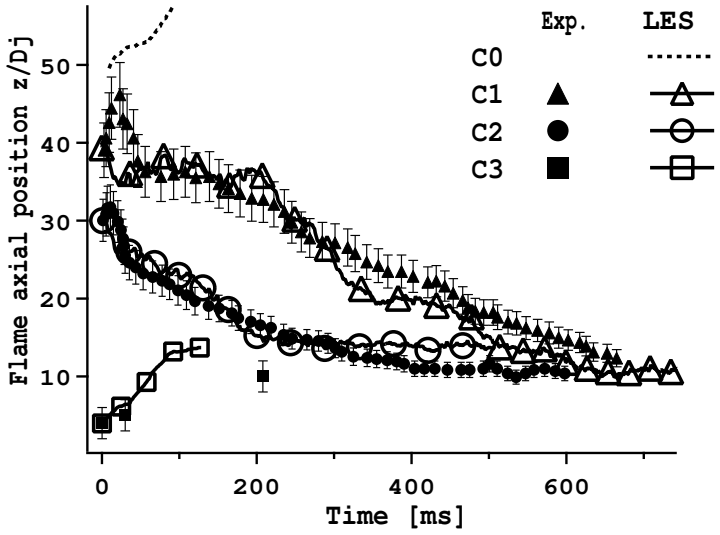

Fig. 16. Axial position of the upstream flame point. Point: experimental measurements of Ahmed and Mastorakos [25] and line: LES. Error bars represent 9% of the mean flame position, which is the maximum error measured in Ref. [25].

The fact that flame position and lift-off height are correctly captured in the LES may be explained by the following observations: (1) cold flow conditions are well reproduced in terms of velocity and mixture fraction distribution; (2) spark ignition and kernel initiation are well represented by the ED model (see next section) and (3) the combustion model performs well in the situation where the combustion mode transitions from a stratified premixed flame to a propagating triple flame (see section 6.3). This third point requires further investigation however, especially to test the influence of greater thickening factors on the stabilization height.

In addition to flame tracking, fast-camera images are compared to LES fields of temperature on Fig. 17 for case C1. The flame topologies are very similar and four phases can be identified in the ignition sequence and in other studies [68,69]. After ignition, a spherical kernel flame appears and is convected downstream (1) (Fig. 17a). Subsequently the kernel expands, (from 0.1 to 15 ms in the LES) keeping an approximately spherical shape (2) (Fig. 17b and c). Finally, the flame propagates upstream against the flow (3) (Fig. 17d, e and f) and stabilizes as an edge flame (4) (Fig. 17g).

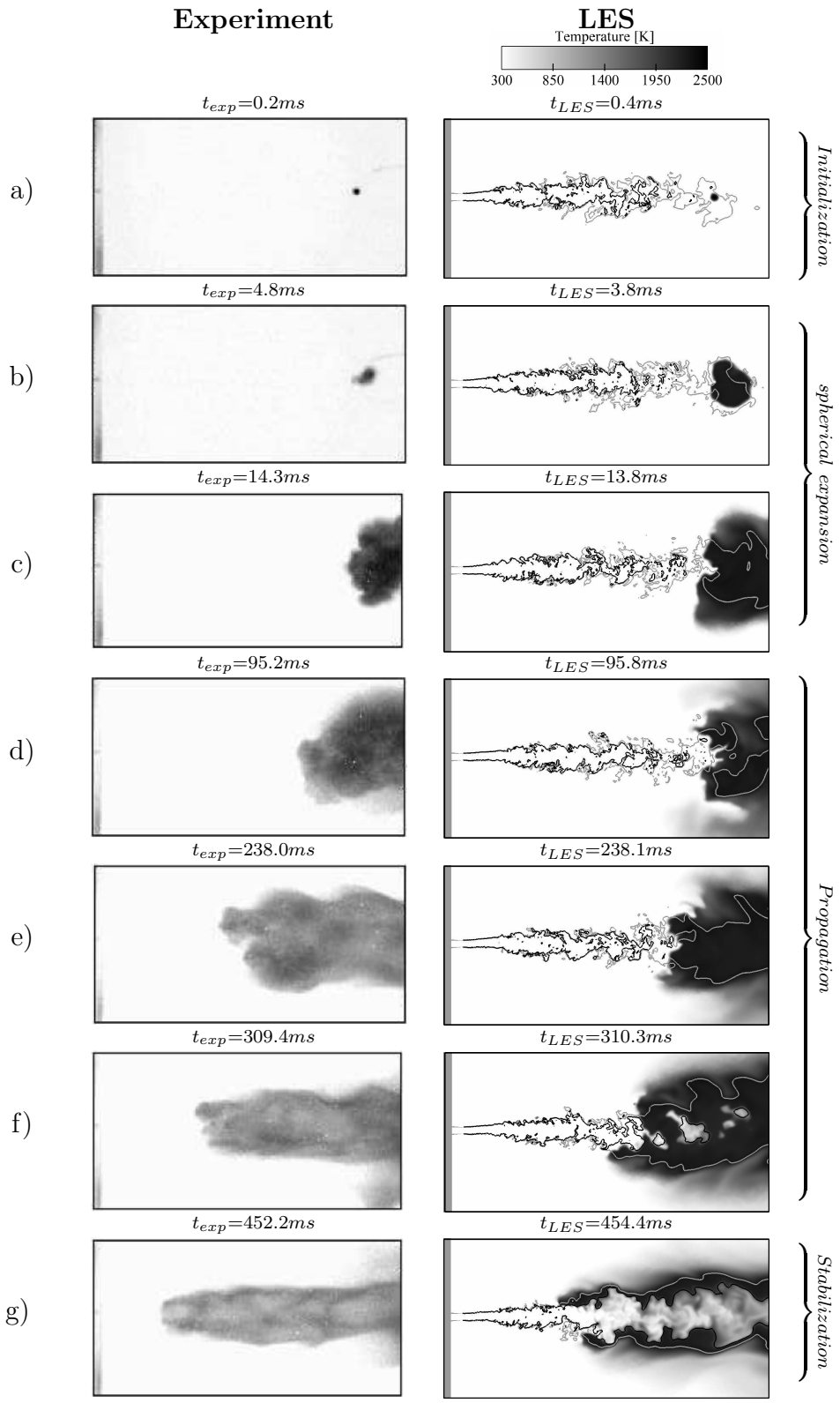

Fig. 17. Comparison of experimental fast-camera images [25] with the instantaneous LES temperature field for the C1 case (times are indicated at the top of each picture). LES results: black line: $\phi = 1.5$ and gray line: $\phi = 1.0$.

Similar experimental and numerical results for the case C3 are compared in Fig. 18. Again for this case, the shape and size of the flame obtained in the LES are in good agreement with experimental pictures.

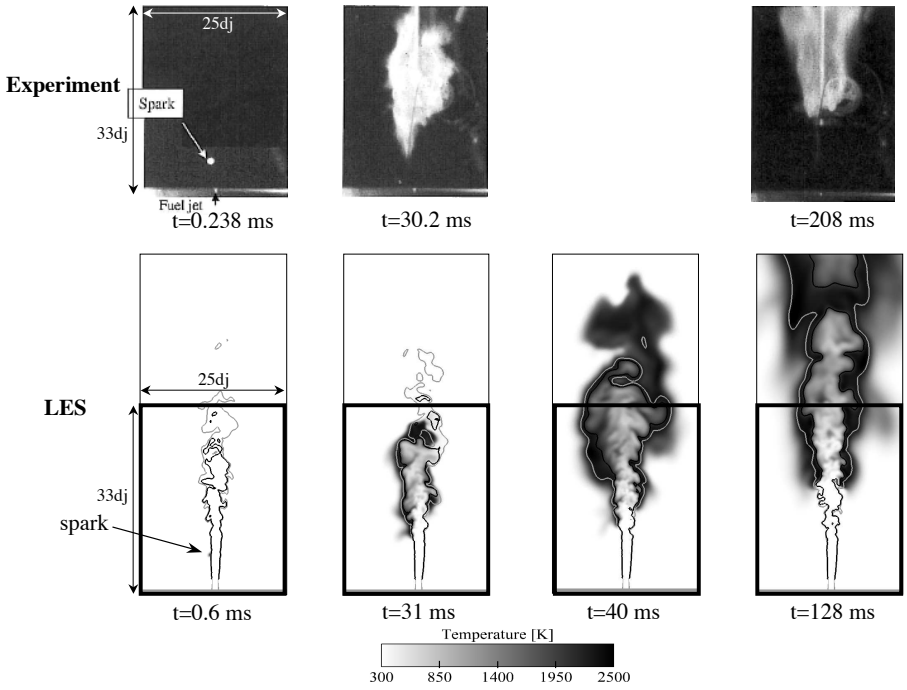

Fig. 18. Ignition at $z/d_j = 4$; $r/d_j = 1$: direct experimental visualizations of the flame [25] compared to computed temperature fields at different times after ignition. For LES results: gray line = stoichiometry and black line = rich flammability limit.

Ahmed and Mastorakos have used OH-PLIF images to characterize the reaction zone [25]. Figure 19 compares the OH-PLIF images with fields of reaction rate obtained with LES for case C1. The flame topologies are comparable in both cases. Ahmed [25] reports that initially the flame has a sphere-like shape (5 ms) and then expands radially (10 ms) before starting to move upstream (30 ms). The same behavior is observed in the LES for the first 30 ms. In the LES the flame wrinkling increases as the flame expands and propagates upstream and this is also observed in experimental results. Ahmed and Mastorakos assumed that the central zone of the flame extinguishes at t=60 ms and at t=100 ms because rich mixture pockets (above the flammability limit) cross the flame front [25]. This event appears in LES results for example at t=143.6 ms.

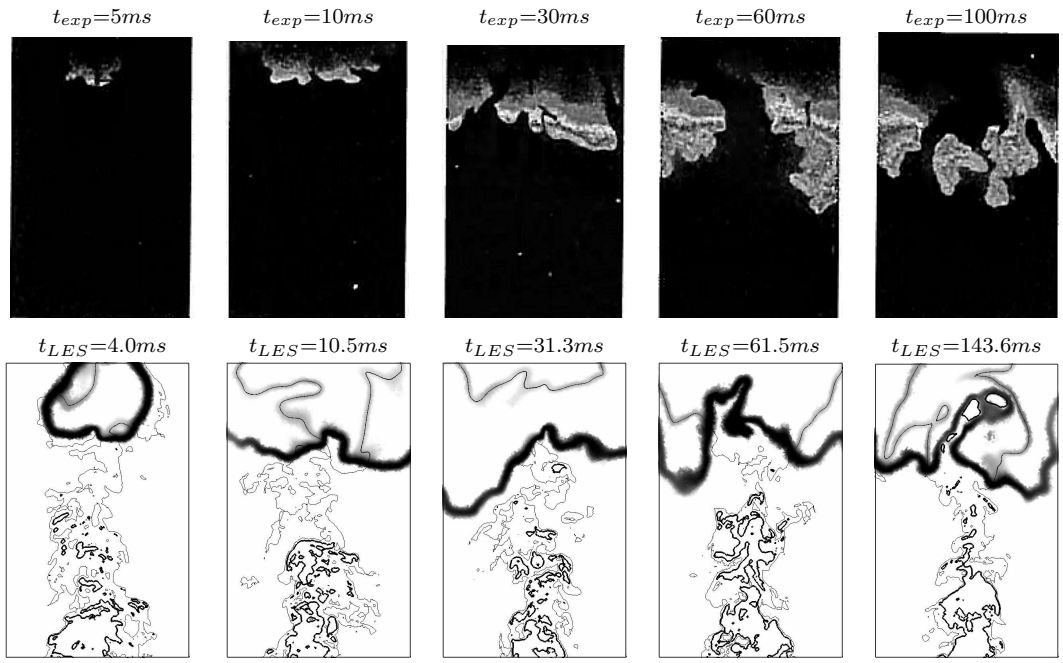

Fig. 19. Comparison between experimental OH-PLIF images [25] (top) and fields of the reaction rate from the LES (bottom) (thick line: rich flammability limit, thin line: stoichiometry). Experimental and numerical results for case C1. The jet flows from bottom to top. For both cases, the imaged region corresponds to 21 d_j and 13 d_j in the axial and radial directions respectively, and the lower side of the images is at z=24 d_j.

6.2 Ignition processes

(1) Flame kernel formation (from 0 to 2 ms)
The flame kernel begins first as a smooth laminar spherical flame. Ahmed and Mastorakos have recorded the temporal evolution of the flame kernel diameter using an average of 10 sets of high speed images in case C2 [25].

From LES results the kernel diameter d_k can be deduced from the volume of burned gases (V_b) assuming that the flame is spherical: $d_k = (6/\pi V_b)^{1/3}$. Figure 20 shows the diameter of the flame kernel in the early instants after ignition in the LES and in the experiment. During this period, the diameter of the flame is larger in the LES than in the experiment but its growth rate is globally well captured.

Early in the ignition process, the flame shape is close to a sphere in both LES and experiment (Fig. 21) . The kernel center stays at the same position in the experiment due to the presence of the electrodes modifying the flow whereas it is convected downstream in the LES when the energy deposition ends.

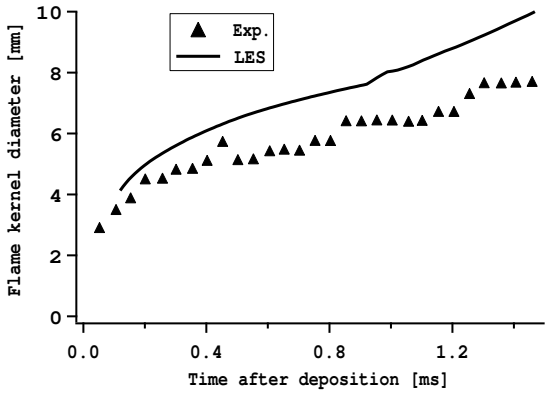

Fig. 20. Kernel growth, comparison between experimental [25] and LES results. Spark location: $z = 30\ d_j$.

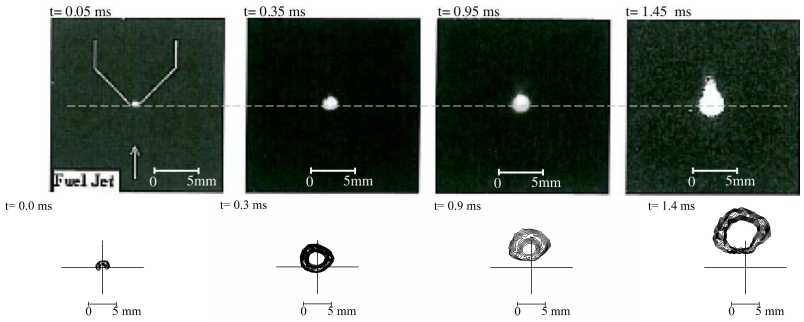

Fig. 21. Growth of the flame kernel. Top: experiment [25], bottom: LES (iso-lines based on heat release).

Note: for the three ignition simulations, the non-reacting initial solutions are chosen in order to have a mixture in the flammable range at the spark location. This point is mainly important for the C2 case where the activation of the ED model in rich mixture pockets leads to weak flame kernels which are rapidly dissipated by turbulent mixing and diffusion effects. No kernel quenching due to turbulence was observed however for these cases.

(2) Quasi-spherical expansion (from 2 to 15 ms)
Just after the kernel formation, the flame expands in all directions in a partially premixed mixture (the mean equivalence ratio at $z \approx 40 d_j$ is about 1.1). As the flame is convected by the mean flow, its expansion is quicker in the downstream direction than towards the injection tube. To evidence the processes involved in this phase, two speeds are defined [1] :

- the absolute flame speed S_f, corresponding to the front speed relative to a

[1] Another speed, the displacement speed S_d, can be defined for perfectly spherical flames: $S_d = \rho_b/\rho_u.dr/dt$ [70,45] (ρ_b and ρ_u are respectively the density of the burned and unburned gases). This expression is not applicable to partially premixed flames and is not used for the present study.

reference frame centered on the kernel. S_f is estimated from an equivalent spherical flame with a volume equal to the burned gas volume:

$$S_f = \frac{dr}{dt} \tag{15}$$

where r is the radius of the equivalent spherical flame, $r = \left(\frac{3}{4\pi}V_b\right)^{1/3}$

- the consumption speed S_c characterizing the speed at which the reactants are consumed. It is calculated from the consumption rate of oxygen:

$$S_c = -\frac{\int \dot{\omega}_{O_2} dv}{\rho_u Y_{O2} \Sigma_{sphere}} \tag{16}$$

where $\dot{\omega}_{O_2}$ is the consumption rate of O_2, ρ_u the density of the unburned gas, Y_{O_2} the mass fraction of O_2 assumed constant in the unburned mixture ($Y_{O_2} \approx 0.215$) and Σ_{sphere} the surface of the equivalent sphere of burned gases.

Figure 22 compares the two speeds and shows that the propagation of the flame from 2 to 15 ms is mainly driven by thermal expansion: the absolute flame speed (S_f) is about five times greater than the consumption speed (S_c) and this factor is close to the density ratio between cold and burned gases: $\rho_b/\rho_u \approx 7.5$.

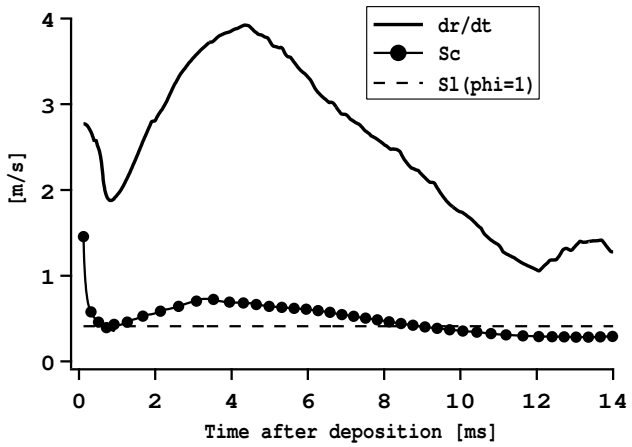

Fig. 22. Consumption speed (S_c) and absolute flame speed ($S_f = \frac{dr}{dt}$) obtained from the LES results. The laminar flame speed at stoichiometry has been added as a reference ($S_l = 0.41\ m/s$).

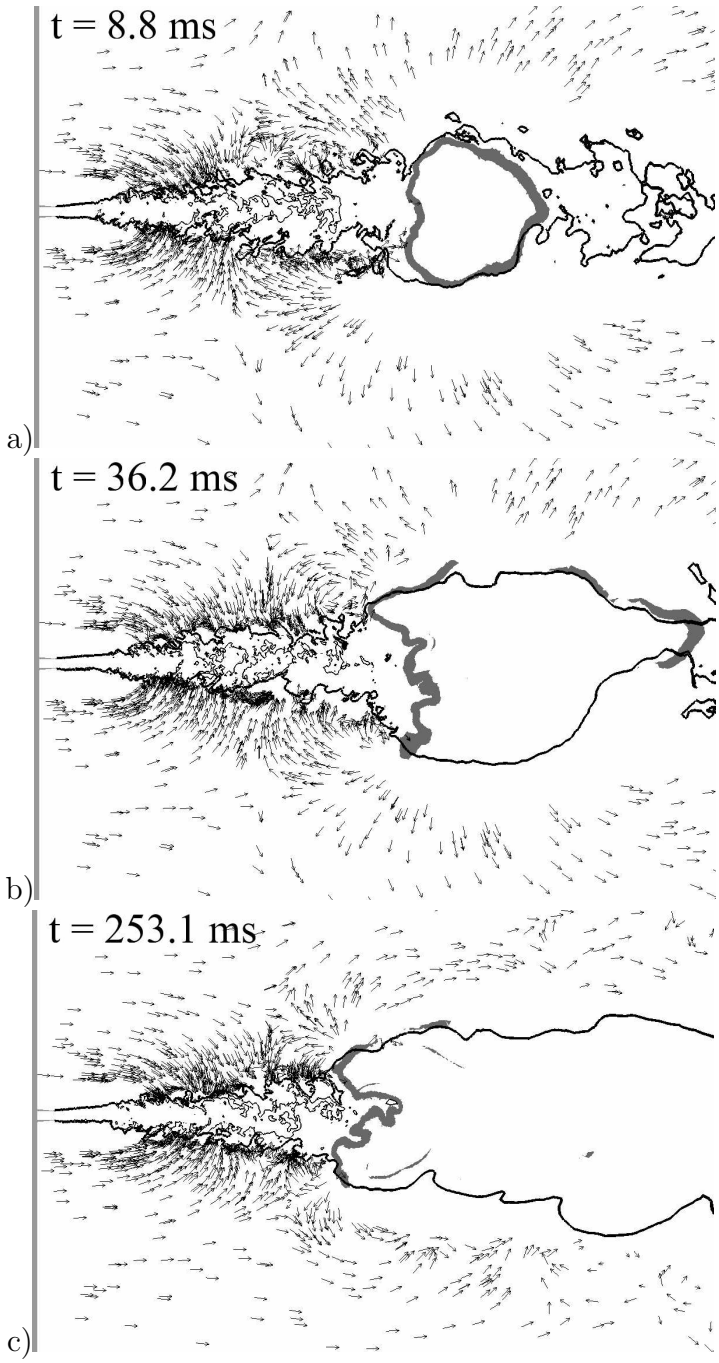

Fig. 23. Propagation phase in the LES. Arrows: velocity ; reactive zone: gray area ; thick line: lean flammability limit and thin line: rich flammability limit.

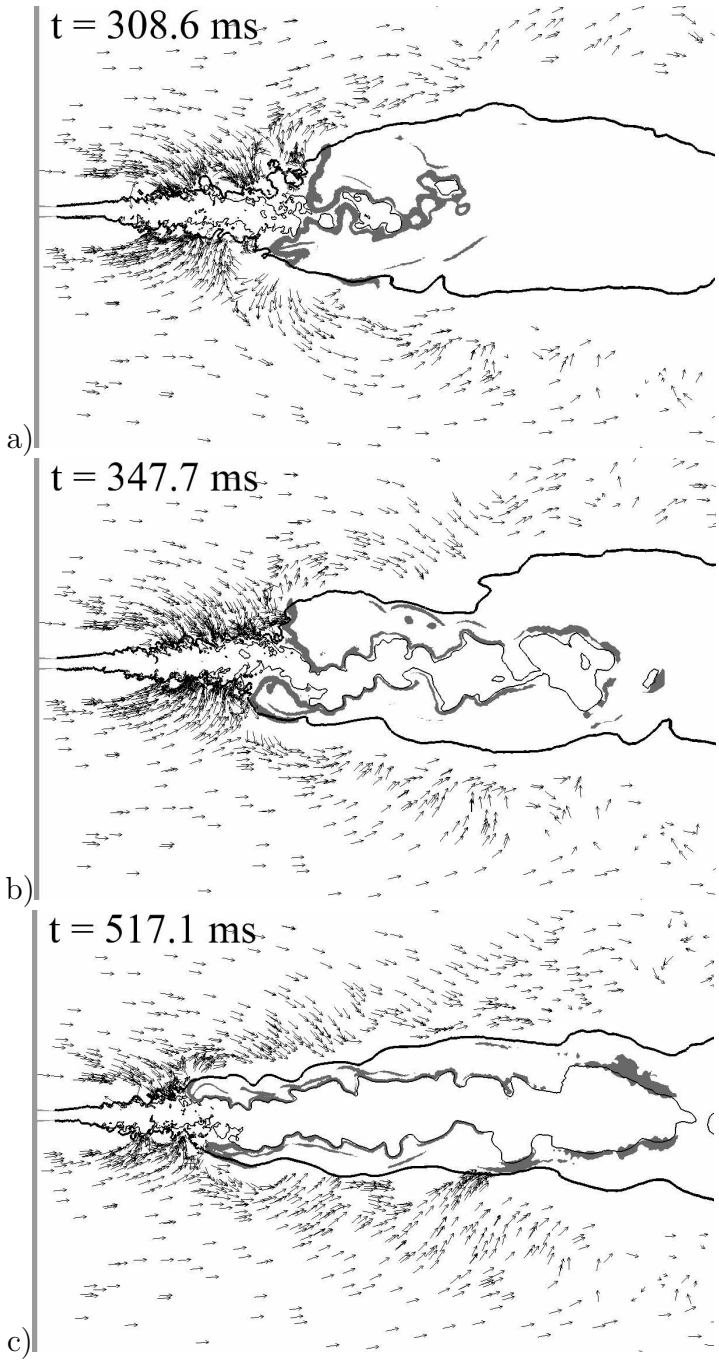

Fig. 24. Propagation phase in the LES. Arrows: velocity ; reactive zone: gray area ; thick line: lean flammability limit and thin line: rich flammability limit.

Figure 23 presents the impact of flame growth and propagation on the jet dynamics. Figure 23a for example confirms that the turbulent spherical flame induces an expansion of the flow.

(3) Upstream propagation of the flame (from 15 to 500 ms)
The spherical propagation of the flame and the rapid expansion of hot gases strongly modify the flow. Figure 23b shows that at $t = 36.2\ ms$ the reactive zone is no longer closed, due to lean extinction in the side regions of the jet. The upstream reactive region is strongly wrinkled in its center by the jet dynamics. The flame propagates upstream by the progression of the flame in the edge region of the jet (Fig. 23c, at $t = 253.1\ ms$), where the flow velocity in the streamwise direction is low and the mixture is close to stoichiometric conditions. In this region, the flow dilatation induced by the flame further reduces the speed of the oncoming flow ahead of the flame. Figure 24a shows that, at $t = 308.6\ ms$, the flame extinguishes in the jet axis region as it encounters rich mixtures. The shape of the flame becomes tubular as its center quenches (Fig. 24b). As the flame becomes cylindrical, the obstruction posed by the flame (Fig. 24a) reduces and the average radius of the flame tube decreases as observed experimentally (Fig. 17f, g and h). As the flame gets closer to the injection tube, less fuel-air premixing occurs, leading to greater penetration of the jet's rich core into the flame (Fig. 24 a, b and c). At $t = 517.1\ ms$ (Fig. 24c), the flame is stabilized by a ring shaped turbulent edge-flame.

To determine the flame regime (premixed or/and diffusion), the Takeno index [71]: $\Upsilon = \nabla Y_{O2}.\nabla Y_{CH4}$ and the indexed reaction rate (based on the one step scheme): $\dot{\omega}^* = \dot{\omega}\frac{\Upsilon}{|\nabla Y_{O2}.\nabla Y_{CH4}|}$ are used. When $\dot{\omega}^* = +\dot{\omega}$ the gradients of the reactants have the same sign and the flame is premixed; otherwise ($\dot{\omega}^* = -\dot{\omega}$) the flame is a diffusion flame. Figure 25 presents computed snapshots of $\dot{\omega}^*$ at three different times of the upstream propagation phase plotted alongside their respective scatter-plots of reaction rate versus the equivalence ratio.

During the quasi-spherical propagation phase (Fig. 25a), the flame evolves predominantly as a premixed flame but with some diffusion flame close to stoichiometry. 8.8 ms after ignition most of the reaction occurs in lean flame fronts as the flame expands radially towards the lean flammability limit. At t=253.1 ms (Fig. 25b), the flame has started its upstream propagation and three reaction modes can be identified: lean and rich premixed branches and a diffusion zone on the stoichiometric line. This flame is a triple flame [72]. When the flame has reached its stabilization location (Fig. 25c), the lean and rich premixed branches and diffusion flames are very close. At this stage, the flame can be called an edge flame and its stabilization is discussed in the following section. The most intense reaction occurs in the rich branch of the flame.

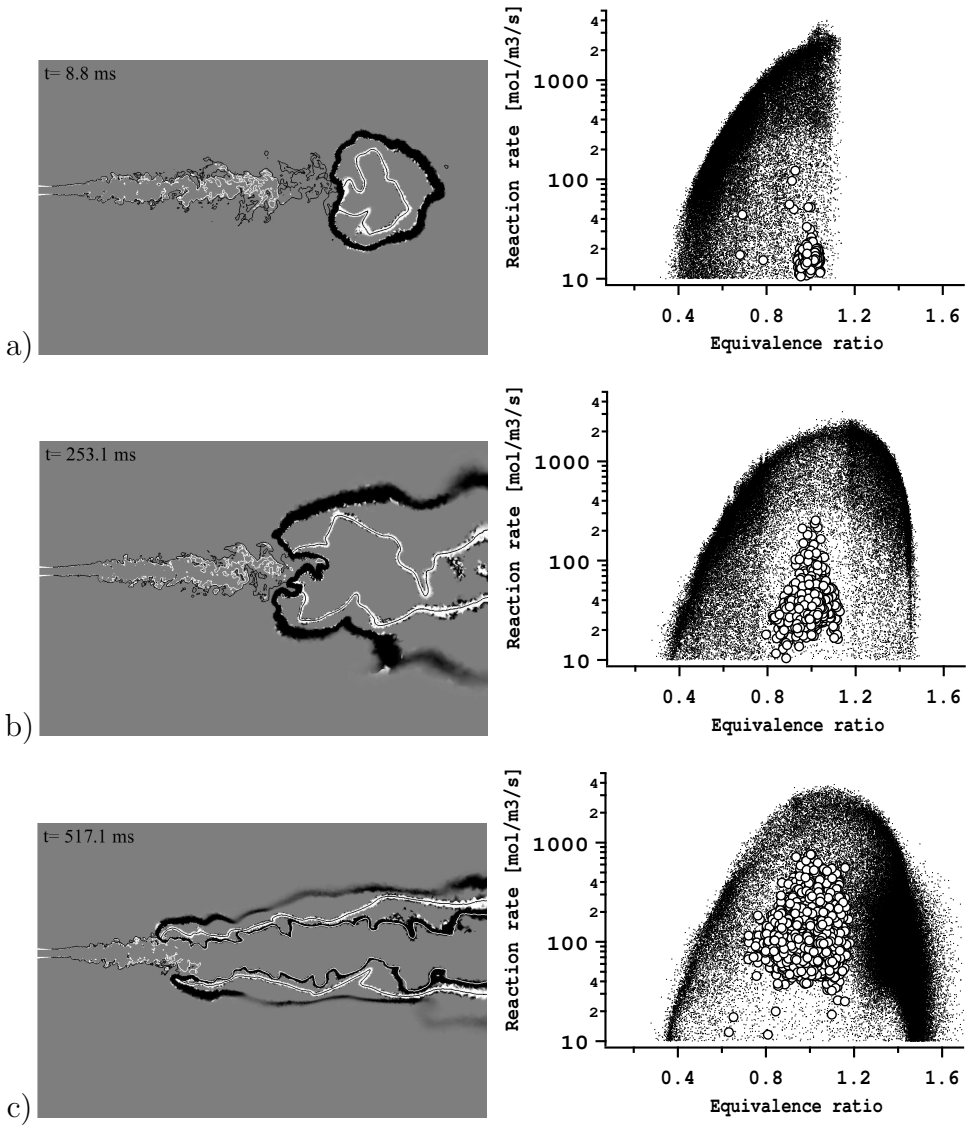

Fig. 25. Combustion regime indicated by the Takeno index [71] (left): black = premixed flame ; white = diffusion flame (black line: stoichiometry, white line: rich flammability limit) and corresponding scatter-plot (right) of the reaction rate of the one-step chemistry versus equivalence ratio (•: premixed regime, ○: diffusion regime).

(4) Stabilization of the edge flame (after 500 ms)
Figure 16 shows that the computed flame for the case C1 stabilizes at approximately 11 d_j downstream of the injector as in the experiment.

Figure 26 displays the velocity field and the Takeno index in the stabilization zone. Figure 26b shows that the flow streamlines diverge approaching the flame. This classical feature of triple flames has been observed in many experimental works [73,74] and is explained by the creation of hot gases which leads to a local dilatation of the flow which assists flame stabilization [73–77].

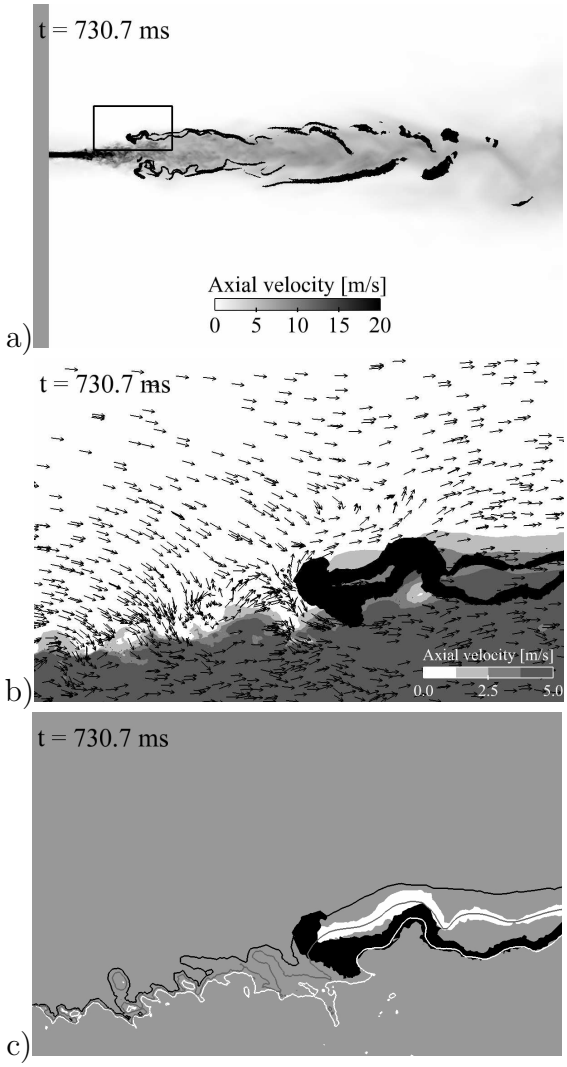

Fig. 26. Stabilization of the lifted flame (the flow is from left to right): (a) region of interest ; (b) flow dynamics around the triple point: black area=reaction zone and arrows: flow direction. (c) Combustion regimes (Takeno index) and flame position relative to the flammability limits (white zone: diffusion flame, black zone: premixed flame ; white line: lean limit, black line: rich limit and gray line: stoichiometric line).

Another aspect of edge flame stabilization is presented in Fig. 26c, where it is shown that the leading edge of the triple flame settles on the stoichiometric line at the intersection of the diffusion and premixed flames; the so-called triple point. The lean premixed branch is rather short compared to the rich premixed one and both premixed fronts stay within the flammability limits as observed experimentally by Schefer et al. [78] and Mansour [79].

The relative axial velocity (V_{rel}) of the fluid flowing across the triple point has been measured from the LES results (Fig. 27). This velocity is defined as: $V_{rel} = V_{flow} - V_{flame}$ where V_{flow} is the axial velocity of the flow recorded along a line parallel to jet axis and passing through the peak reaction rate

in the triple flame; V_{flame} is the axial speed of the flame in the laboratory frame of reference, calculated from the time derivative of the axial position of the flame's leading edge. This method has been employed experimentally by Hasselbrink and Mungal [80] to perform the same analysis using Particle Image Velocimetry (PIV).

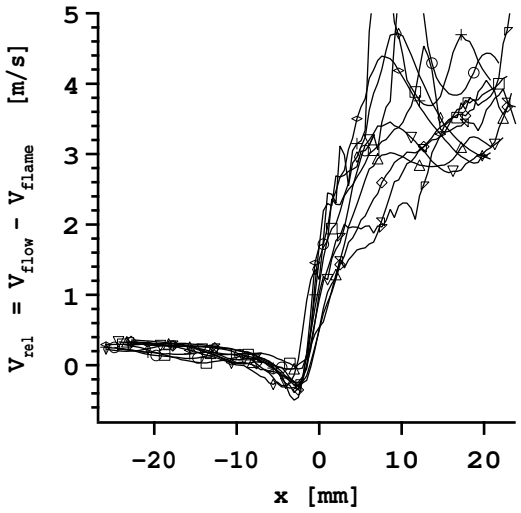

Fig. 27. Relative flow velocity ($V_{rel} = V_{flow} - V_{flame}$) plotted against distance x from the most reactive point for different times.

Figure 27 shows that the flow decelerates ahead of the flame base due to the dilatation and then accelerates in the reaction zone which is consistent with the experimental results of Hasselbrink and Mungal [80] and Schefer and Goix [73]. In the calculation, the relative velocity of the flow at the base of the flame is close to zero and the flame is stabilized in a flow moving at about 0.5 m/s. This result agrees with experimental measurements obtained at comparable Reynolds numbers such as those of Hasselbrink and Mungal [80] and Muñiz and Mungal [74]. These studies concluded that the axial velocity must be low, near the laminar flame speed at stoichiometric conditions ($S^0_{L_{(\phi=1)}} = 0.41\ m/s$) to provide a region for stabilization.

6.3 Impact of the Thickened Flame Model on the triple flame stabilization

To better understand why the flame propagation and the stabilization height are well captured by LES, an analysis of the combustion model parameters is required. Figure 28 presents the field of the thickening factor F (cf. section 2) in the flame stabilization zone. The first point to note is that the flame is resolved while employing a thickening factor less than three. Since the magnitude of the flame thickening is small, and the thickened flame is still much thinner than

the large scale turbulent structures which are important to the upstream flame propagation [26,81], it is anticipated that the flame thickening has limited impact on the flame response.

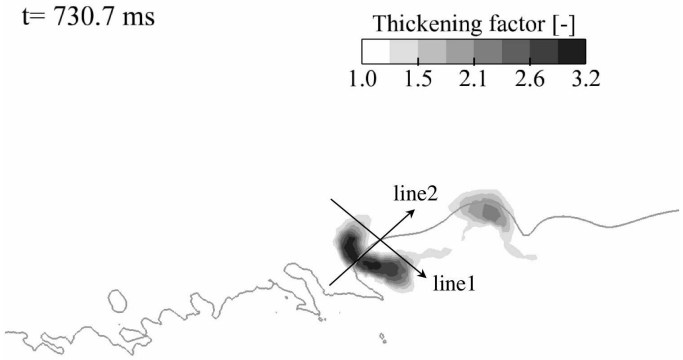

Fig. 28. Field of thickening factor F in the flame stabilization zone (gray line: stoichiometric line).

Second, the combustion model TFLES is activated ($F > 1$) only in the close vicinity of the triple point, on the two premixed branches (cf. Fig. 26c). The TFLES model is not triggered in the diffusion front because reaction rate values in the diffusion branch are about 5 times lower than in premixed regions (as shown in Fig. 29) so that the flame sensor S (constructed as a reaction rate) is not activated in this zone.

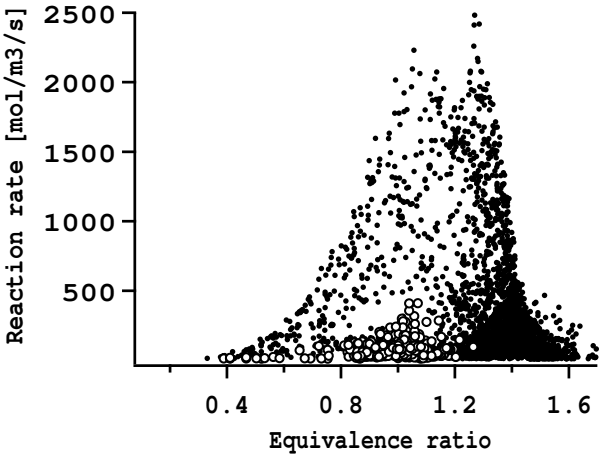

Fig. 29. Scatter plot of the reaction rate in the triple point region (•: premixed regime, ◦ diffusion regime).

This shows that mixing is not affected by the combustion model upstream of the flame front, a necessary condition to capture the stabilization processes [82,83].

Figure 30 presents the values of the thickening factor F and of the efficiency function E (cf. section 2) along two lines across the base of the flame (Fig. 28). Figure 30 shows that the efficiency function E is only activated in the premixed branches (since it depends on thickening) and that its maximum value reaches $E_{max} \approx 1.3$. This result indicates that due to SGS turbulence, the local consumption rate of the flame is only 1.3 times higher than the laminar flame rate. Hence, small scale turbulence has a small impact on the flame speed which agrees with experimental measurements of Watson et al. [83] and Upatnieks et al. [84] causing the flame base to propagate in the flow at a velocity close to the laminar flame speed.

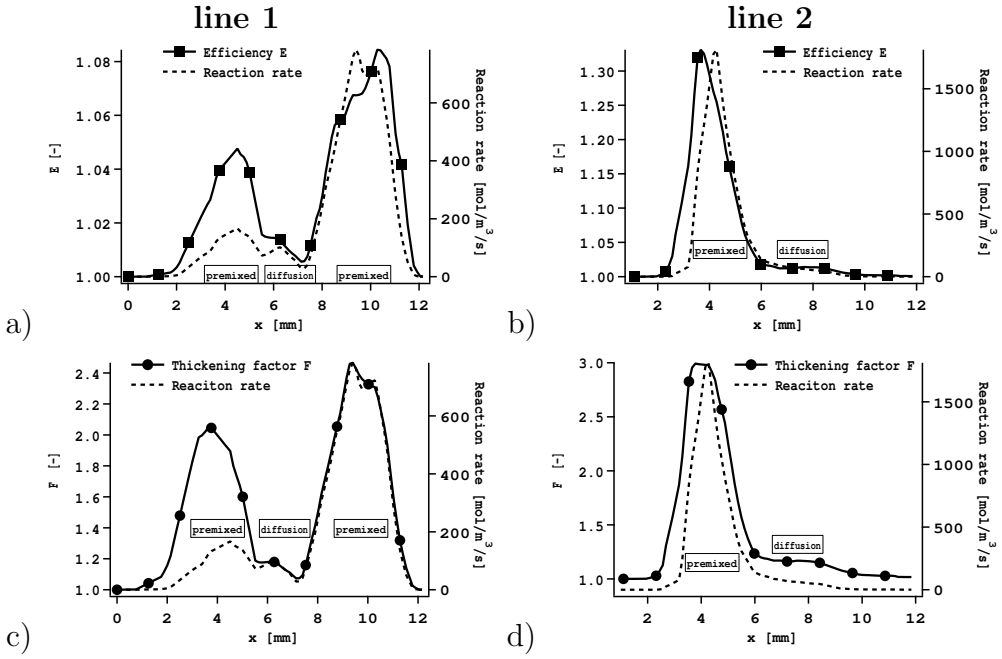

Fig. 30. Parameters of the combustion model (TFLES) along the two lines shown in Fig. 28. Efficiency function E along line 1: subfigure (a) and line 2: subfigure (b). Thickening factor F along line 1: subfigure (c) and 2: subfigure (d).

6.4 Field of ignition probability

Ahmed and Mastorakos established an ignition probability map of the jet [25] using the experimental protocol previously followed by Birch et al. [22] and Smith at al. [23]. For each location, a single spark is triggered 30 times at a rate of 6 sparks per minute to ensure that each test is independent. Three main events can occur after the spark is triggered: (1) no kernel is formed, (2) a kernel is formed but blown-off and (3) a kernel is formed leading to an upstream propagation of the flame and a stabilization as a lifted flame. Only event (3) is considered as a successful ignition in [25] and the ignition probability is then $P_{ig} = J/30$ where J is the number of successful ignitions.

Performing the same ignition probability analysis with LES is prohibited currently by the simulation time requirement. However some statistics based on time analysis of the mixture fraction in the cold flow permit construction of two probabilities from LES data: $P_f(r,\theta,z)$ is the probability of having a flammable mixture at location (r,θ,z) (in a cylindrical coordinate system) and $P_{f|U_c}(r,\theta,z)$ is the probability of having a flammable mixture with an axial speed U_x below a critical value U_c at (r,θ,z). In the experiment [25], the impact of the flow velocity on ignition was studied and it was concluded that for values of U_x above 5.5 m/s at the spark location, ignition fails because of kernel stretching and the increased heat loss due to turbulence [25]. From this result, the value of U_c was set to 5 m/s. Note that $P_{f|U_c}$ is an estimate of the probability of obtaining a kernel from a spark (event (2)) and not the probability of successful ignition (event (3)) denoted P_{ig}.

In the LES, the local equivalence ratio and the velocity of the flow have been recorded at 600 locations in the jet during a total time $\Delta_{t_{tot}}$ of 65 ms. Then the two probabilities can be calculated from:

$$P_f(r,\theta,z) = \frac{1}{\Delta_{t_{tot}}} \int_{\Delta_{t_{tot}}} G(\phi_{(r,\theta,z,t)})dt \tag{17}$$

$$P_{f|U_c}(r,\theta,z) = \frac{1}{\Delta_{t_{tot}}} \int_{\Delta_{t_{tot}}} G(\phi_{(r,\theta,z,t)}) \cdot H(Ux_{(r,\theta,z,t)} - U_c)dt \tag{18}$$

$$\text{with: } G(\phi_{(r,\theta,z,t)}) = H(\phi_{(r,\theta,z,t)} - \phi_{lean}) \cdot [1 - H(\phi_{(r,\theta,z,t)} - \phi_{rich})] \tag{19}$$

where H is the Heaviside function and the limits ϕ_{lean} and ϕ_{rich} are the lean and rich flammability limits respectively.

In Eq. 17 and 18, $\int_{\Delta_{t_{tot}}} G(\phi_{(r,\theta,z,t)})dt$ is the time during which the mixture is flammable and $\int_{\Delta_{t_{tot}}} G(\phi_{(r,\theta,z,t)}) \cdot H(Ux_{(r,\theta,z,t)} - U_c)dt$ is the time during which the mixture is flammable and the axial velocity is below U_c.

Figure 31 presents a comparison (on the jet axis) between P_{ig} the ignition probability measured in the experiment and the two probabilities P_f and $P_{f|Uc}$ obtained from LES results. A first observation is that the regions where $P_f > 0$ and $P_{f|U_c} > 0$, are wider than the region where the average equivalence ratio is flammable as indicated in Fig. 31 by the dashed lines. This can be explained by mixture fluctuations as proposed in Ref. [25,22].

A second result is that the region where $P_{ig} > 0$ is encompassed by the regions where $P_f > 0$ and $P_{f|U_c} > 0$ which is in agreement with the assumption that the formation of a kernel does not necessarily lead to a stable flame.

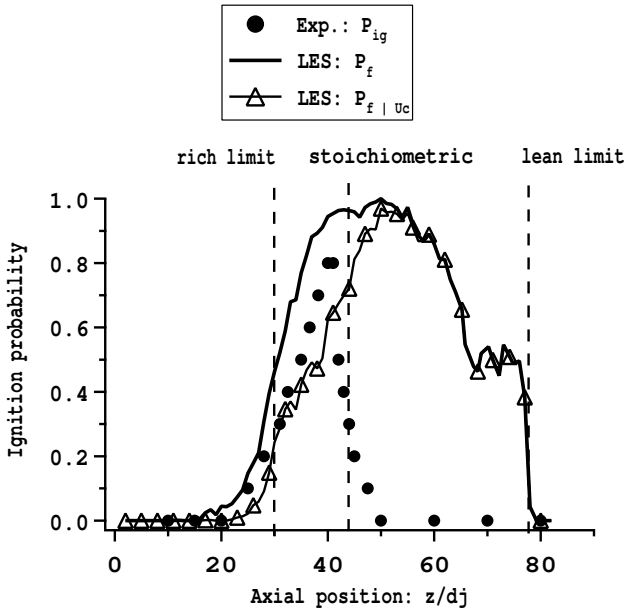

Fig. 31. Ignition probabilities on the jet axis for case C. The experimental value of P_{ig} (points) is plotted with the predicted values of P_f (line) and $P_{f|U_c}$ (line with symbols) from the LES.

In the experiment, $P_{ig} > 0$ in the region between the rich flammability limit and the stoichiometric line and drops to zero when $z > 50d_j$ [25]. Ahmed and Mastorakos [25] observed that P_{ig} falls to zero at $z \approx 50d_j$ (on the jet axis) suggesting that the kernels which form downstream of the location get blown-off. This result has been observed previously by Smith et al. [23]. It was explained in Ref. [25] that since the flame propagates downstream of the spark location following ignition, it encounters lean mixtures resulting in low flame speeds that do not allow the flame to propagate upstream. In the simulation, the ignition triggered at $z = 50\,d_j$ (case C0), generates a kernel but the subsequent flame fails to propagate upstream (Fig.32a). As the spark is located in a lean mixture region, the temperature of the resulting kernel is about 300K lower than in case C1 (Fig.32b) inducing a weaker dilatation of burned gases. This effect coupled with lower consumption speeds make the flame unable to reach the stoichiometric line and yield blow-off.

Figure 33 shows a comparison of the probability (P_{ig}) map measured experimentally [25] and the $P_{f|U_c}$ map reconstructed from cold LES results. In the experiment, the contours have been generated from a matrix of 42×12 points across and along the jet respectively. In the LES the matrix is made of 7 points in the axial direction and 74 points in the transverse direction.

The trends established from Fig. 31 are also observed on Fig. 33: $P_{f|U_c}$ and P_{ig} are relatively close in the $z < 40d_j$ region but $P_{f|U_c}$ remains above zero for $z > 50d_j$ contrary to P_{ig}. As discussed above, this is not surprising since in the present analysis, the LES is post-processed only to predict whether a

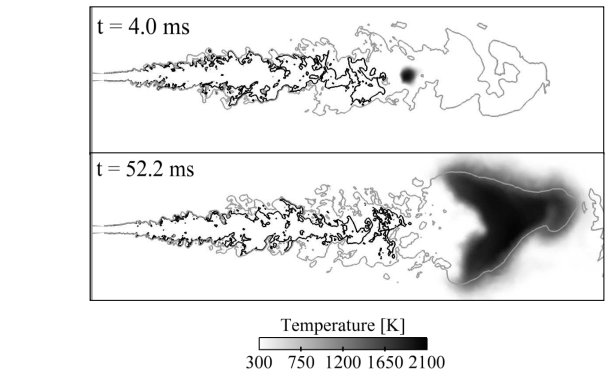

a)

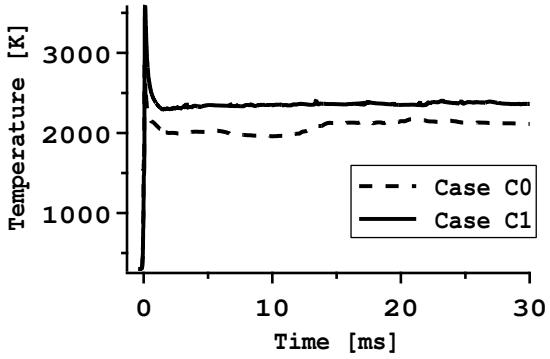

b)

Fig. 32. Ignition case C0: a) flame topology (black line: stoichiometry, gray line: lean flammability limit); b) temporal evolution of the maximum flame temperature for cases C0 and C1.

flame kernel may be formed and not whether a spark might lead to successful ignition.

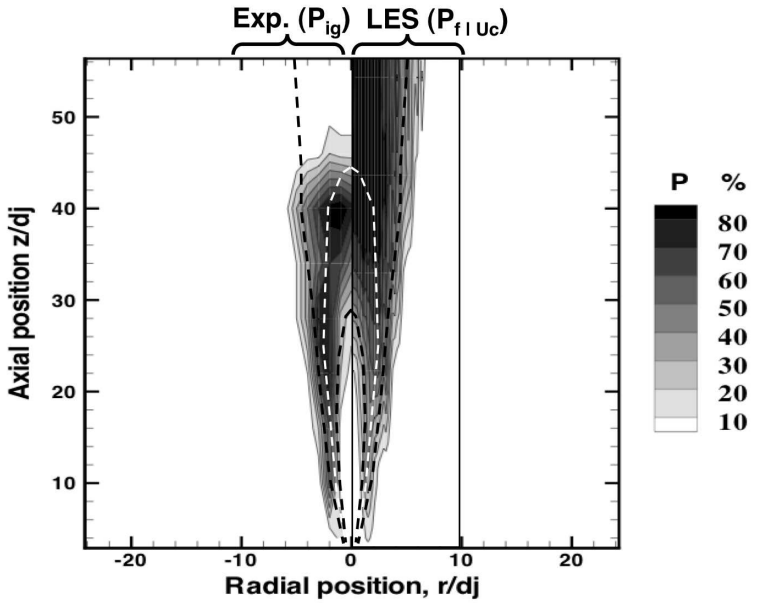

Fig. 33. Ignition probability map: Contours of the experimental ignition probability P_{ig} [25] (left) and $P_{f|U_c}$ predicted from the LES of case B (right). White dashed line: stoichiometric line and black dashed lines: flammability limits (from Eq. 14).

7 Conclusions

In this paper, full ignition sequences of a turbulent non-premixed jet, simulated with a LES approach have been presented. The kernel initiation is explicitly computed by the LES solver owing to a spark ignition model based on energy deposition, making this initial step dependent on the magnitude, duration and location of the energy deposition as well as on mixture and velocity variations at the ignition location. Turbulent combustion has been modeled using a single step chemical scheme coupled to the dynamically Thickened Flame model.

LES results are compared to experimental data reported for the same configuration [25]. Very good agreement is obtained between LES and experimental observations in terms of upstream flame propagation and stabilization as well as flame behavior and topology. Four main phases have been identified in both LES and experiment: (1) kernel initiation, (2) quasi-spherical expansion, (3) rapid upstream propagation and (4) stabilization. During the kernel initiation phase, the energy deposition results in the formation of a flame kernel which is first convected downstream by the jet. During the first phase, the kernel size and growth rate obtained by LES is in good agreement with experiment. Then the flame expands radially as a premixed flame (phase 2). At this time, the growth of the flame is mainly due to thermal expansion, which significantly disrupts the jet dynamics. When the flame reaches the boundaries of the jet, it quenches due to lean conditions and starts to propagate upstream (phase 3). As it gets closer to the jet exit, the flame front encounters mixture beyond

the rich the flammability limit and extinguishes locally. As the flame becomes tubular, a characteristic triple flame shape appears: a diffusion reaction zone on the stoichimetric surface is attached to lean and rich premixed branches. As this triple flame evolves upstream it becomes thinner and stabilizes as an edge flame at 11 diameters of the jet rim (phase 4) as in the experiment.

The probability of obtaining a flame kernel following the spark has also been estimated from LES results using statistics of mixture fraction and velocity in the cold flow. This probability has been compared to the probability of successful ignition, measured experimentally by Ahmed and Mastorakos [25]. The estimate give good accuracy down to the axial extent of the mean stoichiometric iso-surface, where kernel formation has a high probability of leading to a stable flame. Downstream of the mean stoichiometric iso-surface however, kernels which may be viable get blown-off because in the lean mixture, the burned gas expansion is weak and the turbulent flame speed is insufficient to allow upstream propagation.

To complete the comparison with the experiment, additional tests on the impact of the deposited energy amount, of the spark duration and size on ignition processes are necessary. The ignition model must also be validated in configurations with higher strain rates such as counter flow burners, to explore its ability to capture quenching.

8 Acknowledgments

This work was sponsored by the French Space Agency CNES and Snecma (Safran group). This research project has also been supported by a Marie Curie Early Stage Research Training Fellowship of the European Community's Sixth Framework Programme under contract number MEST-CT-2005-020426. The authors also gratefully acknowledge the computing center CINES where most of the calculations were performed, as well as Dr. Mastorakos and the research team of the Engineering Department of Cambridge University for fruitful discussions.

References

[1] E. Mastorakos, *Progress in Energy and Combustion Science* 35 (2009) 57–97.

[2] R. Maly, M. Vogel, in: *17th Symp. (Int.) on Combustion*, The Combustion Institute, Pittsburgh, 1978, pp. 821–831.

[3] R. Teets, J. Sell, *SAE transactions* 97 (1988) 371–383.

[4] P. Ronney, *Opt. Eng.* 33 (1994) 510–521.

[5] T. Phuoc, F. White, *Combustion and Flame* 119 (1999) 203–216.

[6] J.-L. Beduneau, B. Kim, L. Zimmer, Y. Ikeda, *Combustion and Flame* 132 (4) (2003) 653–665.

[7] D. Bradley, C. G. W. Sheppard, I. M. Suardjaja, R. Woolley, *Combustion and Flame* 138 (2004) 55–77.

[8] C. V. Bindhu, S. S. Harilal, M. S. Tillack, F. Najmabadi, A. C. Caeris, *Applied Spectroscopy* 58 (6) (2004) 719–726.

[9] T. Phuoc, F. White, in: *29th Symp. (Int.) on Combustion*, The Combustion Institute, Pittsburgh, 2002, pp. 1621 – 1628.

[10] D. R. Ballal, A. H. Lefebvre, in: *15th Symp. (Int.) on Combustion*, The Combustion Institute, Pittsburgh, 1974, pp. 1473–1481.

[11] C. C. Swett, in: *6th Symp. (Int.) on Combustion*, The Combustion Institute, Pittsburgh, 1956, pp. 523–532.

[12] D. R. Ballal, A. H. Lefebvre, in: *18th Symp. (Int.) on Combustion*, The Combustion Institute, Pittsburgh, 1981, pp. 1737–1747.

[13] P. L. Pitt, R. M. Clements, D. R. Topham, *Combustion Science and Technology* 78 (1986) 289–314.

[14] K. Rao, A. Lefebvre, *Combustion and Flame* 27 (1976) 1–20.

[15] M. Champion, B. Deshaies, G. Joulin, K. Kinoshita, *Combustion and Flame* 65 (3) (1986) 319–337.

[16] M. Champion, B. Deshaies, G. G. Joulin, *Combustion and Flame* 74 (1988) 161–170.

[17] D. Ballal, A. Lefebvre, *Proceedings of the Royal Society of London. Series A* 357 (1977) 163–181.

[18] D. Bradley, F. Lung, *Combustion and Flame* 69 (1) (1987) 71–93.

[19] C. Huang, S. Shy, C. Liu, Y. Yan, in: *31st Symp. (Int.) on Combustion*, The Combustion Institute, Pittsburgh, 2007, pp. 1401–1409.

[20] S. Rashkovsky, in: *First Mediterranean Combustion Symposium, Antalya, Turkey*, 1999.

[21] E. Richardson, E. Mastorakos, *Combustion Science and Technology* 179 (1-3) (2007) 21–37.

[22] A. D. Birch, D. R. Brown, M. G. Dodson, in: *18th Symp. (Int.) on Combustion*, The Combustion Institute, Pittsburgh, 1981, pp. 1775–1780.

[23] M. Smith, A. Birch, D. Brown, M. Fairweather, in: *21th Symp. (Int.) on Combustion*, The Combustion Institute, Pittsburgh, 1986, pp. 1403–1408.

[24] S. F. Ahmed, R. Balachandran, T. Marchione, E. Mastorakos, *Combustion and Flame* 151 (2007) 366–385.

[25] S. Ahmed, E. Mastorakos, *Combustion and Flame* 146 (2006) 215–231.

[26] K. Lyons, *Progress in Energy and Combustion Science* 33 (2) (2007) 211–231.

[27] C. M. Müller, H. Breitbach, N. Peters, in: *25th Symp. (Int.) On Combustion*, The Combustion Institute, Pittsburgh, 1994, pp. 1099 – 1106.

[28] M. Chen, M. Herrmann, N. Peters, in: *28th Symp. (Int.) on Combustion*, The Combustion Institute, Pittsburgh, 2000, pp. 167–174.

[29] D. Veynante, F. Lacas, S. Candel, *AIAA Journal* 29 (1991) 848–851.

[30] O. Colin, A. Benkenida, C. Angelberger, *Oil and Gas Science Tech.* 58 (1) (2003) 47–62.

[31] E. Richardson, *Ignition modelling for turbulent non-premixed flows.*, Ph.D. thesis, University of Cambridge (2007).

[32] E. Richardson, E. Mastorakos, in: *Third European Combustion Meeting (ECM)*, 2007.

[33] P. E. DesJardin, S. H. Frankel, *Physics of Fluids* 10 (9) (1998) 2298 – 2314.

[34] A. R. Kerstein, *Combustion Science and Technology* 60 (1988) 391.

[35] P. A. McMurthy, S. Menon, A. R. Kerstein, in: *24th Symp. (Int.) on Combustion*, The Combustion Institute, Pittsburgh, 1992, pp. 271 – 278.

[36] S. B. Pope, *Progress in Energy and Combustion Science* 19 (11) (1985) 119–192.

[37] P. Domingo, L. Vervisch, K. Bray, *Combustion Theory and Modelling* 6 (2002) 529–551.

[38] M. Boileau, G. Staffelbach, B. Cuenot, T. Poinsot, C. Bérat, *Combustion and Flame* 154 (1-2) (2008) 2–22.

[39] G. Lacaze, B. Cuenot, T. Poinsot, M. Oschwald, *Combustion and Flame* 156 (6) (2009) 1166–1180.

[40] P. Schmitt, T. J. Poinsot, B. Schuermans, K. Geigle, *Journal of Fluid Mechanics* 570 (2007) 17–46.

[41] A. Sengissen, A. Giauque, G. Staffelbach, M. Porta, W. Krebs, P. Kaufmann, T. Poinsot, in: *31st Symp. (Int.) on Combustion*, The Combustion Institute, Pittsburgh, 2007, pp. 1729–1736.

[42] G. Boudier, L. Y. M. Gicquel, T. Poinsot, D. Bissières, C. Bérat, *Combustion and Flame* 155 (1-2) (2008) 196–214.

[43] N. Lamarque, T. Poinsot, *AIAA Journal* 46 (9) (2008) 2282–2292.

[44] A. A. Aldama, *Lecture Notes in Engineering*, Vol. 49, Springer-Verlag, New York, 1990.

[45] T. Poinsot, D. Veynante, *Theoretical and Numerical Combustion*, R.T. Edwards, 2nd edition., 2005.

[46] F. Nicoud, F. Ducros, *Flow, Turbulence and Combustion* 62 (3) (1999) 183–200.

[47] J. Smagorinsky, *Monthly Weather Review* 91 (1963) 99–164.

[48] P. Chassaing, *Turbulence en mécanique des fluides*, Cépaduès-éditions, Toulouse, France, 2000.

[49] S. B. Pope, *Turbulent flows*, Cambridge University Press, 2000.

[50] G. P. Smith, D. M. Golden, M. Frenklach, N. W. Moriarty, B. Eiteneer, M. Goldenberg, C. T. Bowman, R. K. Hanson, S. Song, J. W. C. Gardiner, V. V. Lissianski, Z. Qin, *GRI Topical Report No. GRI-95/0058*.

[51] E. Fernandez, V. Kurdyumov, A. Liñan, in: *28th Symp. (Int.) on Combustion*, The Combustion Institute, Pittsburgh, 2000, pp. 2125–2131.

[52] G. Boudier, L. Y. M. Gicquel, T. Poinsot, D. Bissières, C. Bérat, in: *31st Symp. (Int.) on Combustion*, The Combustion Institute, Pittsburgh, 2007, pp. 3075–3082.

[53] O. Colin, F. Ducros, D. Veynante, T. Poinsot, *Physics of Fluids* 12 (7) (2000) 1843–1863.

[54] F. A. Williams, *Combustion Theory*, Benjamin Cummings, Menlo Park, CA, 1985.

[55] T. D. Butler, P. J. O'Rourke, in: *16th Symp. (Int.) on Combustion*, The Combustion Institute, 1977, pp. 1503 – 1515.

[56] C. Angelberger, F. Egolfopoulos, D. Veynante, *Flow, Turbulence and Combustion* 65 (2) (2000) 205–22.

[57] J.-P. Légier, T. Poinsot, D. Veynante, in: *Proceedings of the Summer Program*, Center for Turbulence Research, NASA Ames/Stanford Univ., 2000, pp. 157–168.

[58] C. Martin, L. Benoit, Y. Sommerer, F. Nicoud, T. Poinsot, *AIAA Journal* 44 (4) (2006) 741–750.

[59] A. Sengissen, J. F. V. Kampen, R. Huls, G. Stoffels, J. B. W. Kok, T. Poinsot, *Combustion and Flame* 150 (2007) 40–53.

[60] C. Vázquez-Espí, A. Liñán, *Combustion Theory and Modelling* 6 (2) (2002) 297–315.

[61] N. Chakraborty, R. S. Mastorakos, E. Cant, *Combustion Science and Technology* 179 (1-3) (2007) 293–317.

[62] T. A. Spiglanin, A. Mcilroy, E. W. Fournier, R. B. Cohen, J. A. Syage, *Combustion and Flame* 102 (3) (1995) 310–328.

[63] V. Erard, A. Boukhalfa, D. Puechberty, M. Coria-Ura, *Combustion Science and Technology* 113 (1) (1996) 313–327.

[64] S. Tieszen, D. Stamps, T. O'Hern, *Combustion and Flame* 106 (1996) 442–466.

[65] J. McQuaid, W. Wright, *International journal of heat and mass transfer* 17 (1974) 341–349.

[66] S. Corrsin, M. Uberoi, *Further experiments on the flow and heat transfer in a heated turbulent air jet*, National Advisory Committee for Aeronautics, 1949.

[67] C. Richards, W. Pitts, *Journal of Fluid Mechanics* 254 (1993) 417–435.

[68] O. Gurliat, V. Schmidt, O. Haidn, M. Oschwald, *Aerospace Science and Technology* 7 (7) (2003) 517–531.

[69] R. W. Bilger, S. B. Pope, K. N. C. Bray, J. F. Driscoll, in: *30th Symp. (Int.) on Combustion*, The Combustion Institute, Pittsburgh, 2005, pp. 21–42.

[70] D. R. Dowdy, D. B. Smith, S. C. Taylor, in: *23rd Symp. (Int.) on Combustion*, The Combustion Institute, Pittsburgh, 1990, pp. 325–332.

[71] H. Yamashita, M. Shimada, T. Takeno, in: *26th Symp. (Int.) on Combustion*, The Combustion Institute, Pittsburgh, 1996, pp. 27 – 34.

[72] H. Phillips, in: *10th Symp. (Int.) on Combustion*, The Combustion Institute, Pittsburgh, 1965, pp. 1277–1283.

[73] R. W. Schefer, P. Goix, *Combustion and Flame* 112 (1998) 559–570.

[74] L. Muñiz, M. G. Mungal, *Combustion and Flame* 111 (1-2) (1997) 16–31.

[75] G. R. Ruetsch, L. Vervisch, A. Liñan, *Physics of Fluids* 7 (6) (1995) 1447–1454.

[76] J. Buckmaster, in: *27th Symp. (int.) on Combustion*, The Combustion Institute, Pittsburgh, 1996, pp. 1143–1149.

[77] J. Buckmaster, *Progress in Energy and Combustion Science* 28 (5) (2002) 435–475.

[78] R. W. Schefer, M. Namazian, J. Kelly, *Combustion and Flame* 99 (1994) 75–86.

[79] M. Mansour, *Combustion and Flame* 133 (3) (2003) 263–274.

[80] E. F. Hasselbrink, M. G. Mungal, in: *27th Symp. (Int.) on Combustion*, The Combustion Institute, Pittsburgh, 1998, pp. 867–874.

[81] J. E. Broadwell, W. J. Dahm, M. G. Mungal, in: *20th Symp. (Int.) on Combustion*, The Combustion Institute, Pittsburgh, 1984, pp. 303 – 310.

[82] H. Eickhoff, B. Lenze, W. Leuckel, in: *20th Symp. (Int.) on Combustion*, The Combustion Institute, Pittsburgh, 1984, pp. 311–318.

[83] K. Watson, K. Lyons, J. Donbar, C. Carter, *Combustion and Flame* 123 (2000) 252–265.

[84] A. Upatnieks, J. F. Driscoll, C. Rasmussen, S. Ceccio, *Combustion and Flame* 138 (2004) 259–272.

[85] A. Van Maaren, D. S. Thung, L. R. H. De Goey, *Combustion Science and Technology* 96 (4) (1994) 327–344.

[86] C. M. Vagelopoulos, F. Egolfopoulos, in: *27th Symp. (Int.) on Combustion*, The Combustion Institute, Pittsburgh, 1998, pp. 513–519.

[87] M. I. Hassan, K. T. Aung, G. M. Faeth, *Combustion and Flame* 115 (4) (1998) 539–550.

[88] X. J. Gu, M. Z. Haq, M. Lawes, R. Woolley, *Combustion and Flame* 121 (2000) 41–58.

[89] I. Wygnanski, H. Fiedler, *Journal of Fluid Mechanics* 38 (03) (1969) 577–612.